



# Adsorption and Photo-Fenton Degradation of Methylene Blue Using Nanomagnetite/Potassium Carrageenan Bio-Composite Beads

Asaad F. Hassan<sup>1</sup> · Ahmed A. Mustafa<sup>1</sup> · Ghada Esmail<sup>1</sup> · Aya M. Awad<sup>1</sup>

Received: 23 March 2022 / Accepted: 16 June 2022 / Published online: 22 July 2022  
© The Author(s) 2022

## Abstract

The present study deals with the preparation of nanomagnetite (NM), potassium carrageenan (KC), and nanomagnetite/potassium carrageenan bio-composite beads (NC). Characterization of the prepared solid materials using different physicochemical techniques such as X-ray diffraction analysis (XRD), thermogravimetric analysis (TGA), scanning electron microscopy (SEM), transmission electron microscope (TEM), energy-disperse X-ray spectroscopy (EDX), diffuse reflectance spectrophotometer (DRS), swelling ratio (SR%), N<sub>2</sub> adsorption, pH of point of zero charges (pH<sub>PZC</sub>), and Fourier transform infrared spectroscopy (FTIR). Comparing between adsorption and photo-Fenton degradation process for methylene blue (MB) on the surface of the prepared solid materials. Nanomagnetite/potassium carrageenan bio-composite (NC) exhibited high specific surface area (406 m<sup>2</sup>/g), mesoporosity (pore radius, 3.64 nm), point of zero charge around pH6.0, and the occurrence of abundant oxygen-containing functional groups. Comparison between adsorption and photo-Fenton oxidation process for methylene blue (MB) was carried out under different application conditions. NC exhibited the maximum adsorption capacity with 374.50 mg/g at 40 °C after 24 h of shaking time while 96.9% of MB was completely degraded after 20 min of photo-Fenton process. Langmuir's adsorption model for MB onto the investigated solid materials is the best-fitted adsorption model based on the higher correlation coefficient values (0.9771–0.9999). Kinetic and thermodynamic measurements prove that adsorption follows PSO, endothermic, and spontaneous process, while photo-Fenton degradation of MB achieves PFO, nonspontaneous, and endothermic process. Photo-Fenton degradation is a fast and simple technique at a lower concentration of dye (< 40 mg/L) while at higher dye concentration, the adsorption process is preferred in the removal of that dye.

**Keywords** Kappa-carrageenan · Nanomagnetite · Composite · Adsorption · Fenton · Reusability

## 1 Introduction

Owing to the rapid advancement of technology, industry, and urbanization, large amounts of toxins that threaten microorganisms, animals, and plant life even at low concentrations have been released into the aquatic environment [1, 2]. Among all of these pollutants, synthetic dyes predominantly are used in the textile industry including dyeing and printing processes [3]. Synthetic dyes are the most dangerous pollutants to the aquatic environment that decrease photosynthesis, the percentage of oxygen dissolved in water, and easily remain in the cells of all living organisms [4]. Dyes are categorized into anionic, cationic, and nonionic according

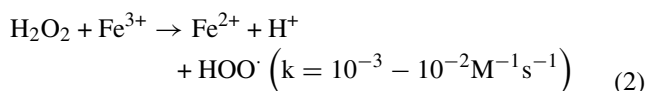
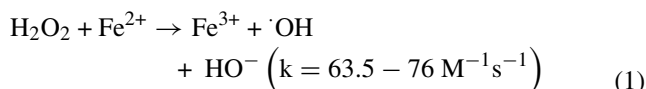
to their chemical structure. Methylene blue (MB) is considered one of the most dangerous basic cationic dyes [5]. It is a poisonous, heterocyclic, phenothiazine dye with a limit value that must be < 0.2 mg/L in water according to the Environmental Protection Agency (EPA) [6]. MB causes many diseases such as mental disorders [7], vomiting, nausea, paralysis, hypertension, and methemoglobinemia [8]. It is difficult to remove MB from ecosystems due to the presence of three rings in its aromatic structure, high stability, and resistance to biodegradability [9]. Different biological and physicochemical methods for the removal of MB have been investigated including adsorption [10], coagulation, filtration, reverse osmosis [11], reduction, and oxidation [12]. Biological treatment of dyes in the aquatic medium is not the recommended method due to the formation of more toxic intermediate which requires many additional removal methods [13]. As a result, advanced oxidation processes (AOPS) are the best techniques for water treatment such as ozonation,

✉ Asaad F. Hassan  
asmz68@sci.dmu.edu.eg; asmz68@yahoo.com

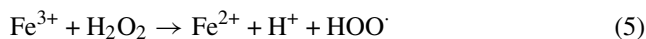
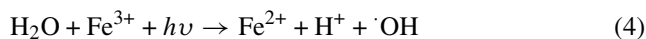
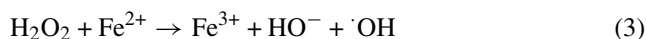
<sup>1</sup> Chemistry Department, Faculty of Science, Damanhour University, Damanhour, Egypt



chlorination, and Fenton process [8, 14]. Ozonation and chlorination are not common oxidation methods because of the short lifetime of ozone and the toxicity of chlorine while the Fenton process is regarded as the most innovative method for the degradation of organic pollutants [15]. In 1894 Fenton reaction was discovered by Henry Fenton for tartaric acid oxidation by the reaction between Fenton's reagent (ferrous ion and hydrogen peroxide) to produce hydroxyl radical ( $\cdot\text{OH}$ ) which is a very reactive and general strong oxidant with higher oxidation potential equals 2.8 eV [16]. It can oxidize organic contaminants into safe  $\text{H}_2\text{O}$  and  $\text{CO}_2$  as indicated by the Haber–Weiss mechanism [17]:



Although heterogeneous and homogenous applications of the Fenton process are possible, heterogeneous Fenton has significant advantages over homogeneous ones in terms of increasing iron activity, reducing the generation of sludge, and the high efficiency of  $\text{H}_2\text{O}_2$ . Since the rate of reaction in the classical Fenton decreases with time, external energy such as ultraviolet radiation (UV) is needed to speed up the degradation in photo-Fenton reaction by raising the decomposition of  $\text{H}_2\text{O}_2$  to hydroxyl radical, converting ferrous to ferric ion [18, 19], and the activation of solid semiconductor nanocatalyst leads to the formation of electron–hole pair ( $e^- - h^+$ ) which increases the degradation of MB with another faster reaction pathways as indicated in the following equations:



Because of the unique properties of nanocatalysts as their high specific surface area to volume ratio, small size, their high removal efficiency, they have been introduced into the field of photocatalysis. Nanomagnetite ( $\text{Fe}_3\text{O}_4$ ) is considered an effective photocatalyst in the photo-Fenton process, it is a superparamagnetic semiconductor that contains both ferric and ferrous ions in its structure with a bandgap of about 0.14 eV, so it is the most powerful material to remove dyes. Nanomagnetite is characterized by low toxicity, ease of handling and synthesis, friendliness to the environment, and stability of its chemical structure [20, 21]. The difficult separation of

nanomagnetite from the application medium promotes the formation of a new bio-composite with another biopolymer to enhance its oxidation power and facilitate its separation. Photo-Fenton degradation of MB was studied using different composites such as  $\text{Au-Fe}_3\text{O}_4/\text{graphene}$ ,  $\text{MnFe}_2\text{O}_4/\text{g-C}_3\text{N}_4$ ,  $\beta\text{-NiOOH/FeMoO}_4$ , and  $\text{CuFe}_2\text{O}_4\text{-Fe}_2\text{O}_3$  [22–25].

This research work aims to perform a comparative study between adsorption and catalytic heterogeneous photo-Fenton process in the presence of a newly synthesized bio-composite (nanomagnetite/carrageenan composite). Different physicochemical techniques were investigated for full characterization of all synthesized solid adsorbents including FTIR, SEM, TEM,  $\text{N}_2$  adsorption, EDX, DRS, XRD, and TGA. Different application conditions such as the effect of adsorbent dosage, pH of the solution, application time, initial MB concentration, and the effect of temperature were studied during adsorption and Fenton oxidation treatment.

## 2 Materials and Methods

### 2.1 Materials

Ferrous chloride tetrahydrate and ferric chloride hexahydrate were obtained from Oxford Lab Fine Chem LLP, India. Methylene blue and kappa-carrageenan were purchased from Sigma-Aldrich Co., USA. Hydrogen peroxide (50%), potassium chloride ( $\geq 99\%$ ), sodium hydroxide ( $\geq 98\%$ ), hydrochloric acid, and concentrated ammonium hydroxide (28%) were purchased from El-Nasr for pharmaceutical and chemical industrial Co., Egypt. All of these reagents were utilized without extra purification.

### 2.2 Preparation of solid Materials

#### 2.2.1 Preparation of Nanomagnetite (NM)

Magnetite nanoparticles were prepared by mixing 2.21 g of  $\text{FeCl}_2 \cdot 4\text{H}_2\text{O}$  and 5.82 g of  $\text{FeCl}_3 \cdot 6\text{H}_2\text{O}$  (1:2 molar ratio) in 175 mL of distilled water using a three-neck flask under  $\text{N}_2$  gas, followed by heating the final mixture using a magnetic stirrer at 80 °C, then 15 mL of  $\text{NH}_4\text{OH}$  (28%) was added as one dosage. The black-colored solution that resulted was heated at the same temperature for about 10 minutes. The solution was filtered, and the black precipitate was washed by distilled water and dried in an oven at 80 °C [16].

#### 2.2.2 Preparation of Potassium Carrageenan Beads (KC)

Potassium carrageenan beads were prepared by dissolving 10 g of potassium chloride in 100 mL distilled water at room temperature, and dissolving 1 g of kappa-carrageenan in 40 mL distilled water using a hot plate at 80 °C with continuous

stirring. Kappa-carrageenan solution was added drop by drop into the prepared potassium chloride solution using a syringe with continuous magnetic stirring. The final solution was stirred for about 1 h and followed by filtration. The produced crystal beads were washed using distilled water and dried in an oven at 60 °C [26].

### 2.2.3 Preparation of Nanomagnetite Potassium Carrageenan Bio-Composite Beads (NC)

Kappa-carrageenan (1 g) was dissolved in 40 mL distilled water. 1 g of the grinded prepared nanomagnetite particles (NM) were well dispersed into the previous solution and the mixture was heated at 80 °C for about 10 min, then in another beaker, 10 g of potassium chloride was dissolved into 100 mL of distilled water. Using a syringe, nanomagnetite/kappa-carrageenan mixture was added drop by drop into the prepared KCl solution and the final mixture was left for 1 h. The solution was filtered and produced bio-composite beads were washed by distilled water, and finally dried at 90 °C.

## 2.3 Characterization of Prepared Solid Materials

Different physicochemical techniques were carried out to identify the textural, thermal, and chemical properties of all prepared solid materials (NM, KC, and NC). Textural characterization for NM, KC, and NC as specific surface area ( $S_{BET}$ ,  $m^2/g$ ), total pore volume ( $V_T$ ,  $cm^3/g$ ), and pore radius (nm) were investigated by  $N_2$  physisorption using NOVA3200e gas sorption analyzer (Quantachrome Corporation, USA). Before the adsorption process, the solid samples were degassed under vacuum at 180 °C and  $10^{-5}$  Torr overnight to ensure a dry clean solid surface.

The morphological structure of NM and NC as solid adsorbents was determined by scanning electron microscopy (SEM) using a JEOL-JSM-7500 F instrument attached with energy-disperse X-ray spectroscopy (EDX) for the determination of elements on the surface of solid adsorbents, particle size, and shape. Surfaces of the samples were coated with a thin layer of gold (3.5 nm) by the vacuum evaporation technique to minimize sample charging effects due to the electron beam. Transmission electron microscope (TEM) was examined through a JEOL-JEM-2100 (Tokyo, Japan). The samples were dried in an oven at 110 °C and dispersed in anhydrous ethanol solution under ultrasonication for 15 min and a drop of solution was placed on Cu grid followed by coating with lacey carbon film.

X-ray diffraction analysis (XRD) for NM, KC, and NC was performed to study crystal structures and particle size of solid adsorbents via D8 Advance diffractometer. X-ray investigations were applied using a thin powder sample and placed onto an oriented monocrystalline quartz plate for exposure

to Cu K $\alpha$  X-ray source ( $\lambda = 1.5406 \text{ \AA}$ ). The radiation source operates at 40 kV volt and a current of 40 mA with Ni-filtered radiation. The samples were analyzed at room temperature over  $2\theta$  range of  $5^\circ$ – $90^\circ$  with a step size of  $0.02^\circ 2\theta$ .

A diffuse reflectance spectrophotometer (DRS) was applied to determine different band gaps for NM and NC by using a UV–Vis scanning spectrophotometer (JASCO, Japan). The experimental data were obtained by adding a very little weight of dried solid-state samples into the holder of the apparatus. During the preparation of samples for testing, the program instruction of the instrument was followed such as wavelength and intensity. Air was used as the background measurement.

Thermogravimetric analysis (TGA) for NM, KC, and NC was investigated under nitrogen flow rate 20 mL/min with a heating rate of 5 °C/min from room temperature up to 800 °C by SDT Q600 V20.9 Build 20 instrument, UK.

Fourier transform infrared (FTIR) spectroscopy for all the prepared solid materials was investigated using Mattson 5000 FTIR spectrometer, USA, in a range between 400 and 4000  $cm^{-1}$ . Disks were prepared by mixing 5 mg of the dried sample with 0.5 g of potassium bromide (with ratio 1:500) in an agate mortar, pressing the mixture at 7 ton/ $cm^3$  for 5 min and 10 ton/ $cm^3$  for 7 min. Point of zero charges for NM, KC, and NC were studied by adding 35 mL of 0.1 mol/L sodium chloride solutions in several capped bottles with 0.1 g of the prepared solid materials and pH values were adjusted to obtain a pH range from (2–11) using HCl and/or NaOH (0.1 mol/L). The bottles were shaken for about 48 h, the values of  $pH_{final}$  were determined by pH meter and  $pH_{PZC}$  is defined as the point at which  $pH_{final} - pH_{initial}$  equals zero [27].

## 2.4 Static Adsorption of Methylene Blue

Batch experiments for adsorption of MB onto the surface of NM, KC, and NC were performed through various application conditions to determine the maximum adsorption capacities, the optimum adsorption conditions, thermodynamic, and kinetic parameters.

Adsorption of MB from aqueous solution at the surface of NM, KC, and NC was investigated by mixing 75 mL of MB solution having a known mass of adsorbents (0.1 g) at pH6.5, 30 h as a shaking time at 15 °C. The solution was filtered using the Büchner funnel with Whatman filter paper grade 40, the first five milliliters from filtrate was rejected, and the residual MB concentration was determined by UV-Vis spectrophotometer ( $\lambda_{max}$  663 nm). Equilibrium adsorption capacity ( $q_e$ , mg/g) was determined by the following equation:

$$q_e = \frac{(C_i - C_f) \times V}{W} \quad (6)$$



where  $C_i$  and  $C_f$  (mg/L) are the initial and final concentrations of MB dye in solution, respectively.  $W$  is the mass of adsorbent (g) and  $V$  is the volume of solution (L).

Different conditions of adsorption were studied such as the effect of adsorbent dosage (0.3–2.5 g/L), the effect of initial concentration (10–600 mg/L), time for shaking up to 48 h, pH (2–11), and the effect of temperature (15, 28, and 40 °C). Removal (%) was determined by the following equation:

$$\text{Removal}(\%) = \frac{(C_i - C_f)}{C_i} \times 100 \quad (7)$$

## 2.5 Different Models of Adsorption Isotherm

Various models such as Langmuir, Freundlich, Temkin, and Dubinin–Radushkevich equations were utilized to study the availability of MB adsorption on the surface of solid adsorbents [28, 29].

### 2.5.1 Langmuir Adsorption Model

Langmuir model suggests that adsorption as a monolayer depends on surface homogeneity and Langmuir linear equation is presented as:

$$\frac{C_e}{q_e} = \frac{1}{k_L q_m} + \frac{C_e}{q_m} \quad (8)$$

where  $C_e$  (mg/L),  $q_m$  (mg/g), and  $q_e$  (mg/g) are equilibrium concentration, maximum adsorption capacity, and equilibrium adsorption capacity, respectively.  $K_L$  (L/mg) is Langmuir adsorption constant.

The Langmuir adsorption isotherm can be explained in terms of  $R_L$  (dimensionless separation factor) as discussed by the following equation:

$$R_L = \frac{1}{1 + K_L C_i} \quad (9)$$

where  $C_i$  is the initial concentration of MB (mg/L),  $R_L$  value shows the nature of adsorption to be favorable in case of  $0 < R_L < 1$ , unfavorable when  $R_L$  greater than 1, linear if  $R_L = 1$ , and irreversible in case of  $R_L$  equals zero.

### 2.5.2 Freundlich Adsorption Model

Freundlich's model discusses multilayer adsorption onto a heterogeneous solid surface, where the binding energy of all active sites is different.

$$\text{Ln}q_e = \text{Ln}K_F + \frac{1}{n}\text{Ln}C_e \quad (10)$$

Here in  $K_F$  (L/mg) and  $n$  are related to the adsorption capacity and intensity of adsorption, respectively.

### 2.5.3 Temkin Adsorption Model

The Temkin model explains the interaction between adsorbate and adsorbent by ignoring the high and low concentrations and declining adsorption heat between layers.

$$q_e = B \ln K_T + B \ln C_e \quad (11)$$

$$B = \frac{RT}{b_T} \quad (12)$$

where  $B$ ,  $R$ , and  $T$  are constants related to the adsorption heat, the ideal gas constant (8.314 J mol<sup>-1</sup> · K<sup>-1</sup>), and the absolute temperature (K), respectively.  $K_T$  (L/g) and  $b_T$  (J/mol) are Temkin constants.

### 2.5.4 Dubinin–Radushkevich Adsorption Model

Dubinin–Radushkevich model considers adsorption onto the heterogeneous and homogenous surfaces of adsorbents and can be represented by the following linear equation:

$$\text{Ln}q_e = \text{Ln}(q_{DR}) - (K_{DR}\varepsilon^2) \quad (13)$$

$$\varepsilon = RT \text{Ln}\left(1 + \frac{1}{C_e}\right) \quad (14)$$

For the calculation of mean adsorption energy ( $E_{DR}$ , kJ/mol) Eq. 15 is utilized:

$$E_{DR} = \frac{1}{\sqrt{2K_{DR}}} \quad (15)$$

where  $K_{DR}$  (mol<sup>2</sup>/kJ<sup>2</sup>),  $q_{DR}$  (mg/g), and  $\varepsilon$  are the activity coefficient, maximum adsorption capacity, and Polanyi adsorption potential, respectively.

## 2.6 Kinetic Models for Adsorption Process

Various kinetic models (Eqs.16–18) were utilized for studying kinetic parameters of MB adsorption on the surface of prepared solid adsorbents [30–32].

Pseudo-first-order (PFO) kinetic model:

$$\text{Ln}(q_e - q_t) = \text{Ln}q_e - k_1 t \quad (16)$$

Pseudo-second-order (PSO) kinetic model:

$$\frac{t}{q_t} = \frac{1}{k_2 q_e^2} + \frac{t}{q_e} \quad (17)$$



Elovich kinetic model:

$$q_t = \frac{\ln \alpha \beta}{\beta} + \frac{\ln t}{\beta} \quad (18)$$

where  $k_1$  ( $\text{h}^{-1}$ ),  $k_2$  ( $\text{g}/\text{mg}^{-1}$ ), and  $q_t$  ( $\text{mg}/\text{g}$ ) are PFO rate constant, PSO rate constant, and adsorption capacity at time ( $t$ ), respectively.  $\alpha$  ( $\text{mg}/\text{g h}^{-1}$ ) and  $\beta$  ( $\text{g}/\text{mg}$ ) are the initial rate of MB adsorption and activation energy of adsorption, respectively.

Adsorption capacity  $q_t$  ( $\text{mg}/\text{g}$ ) at a certain time ( $t$ ) can be calculated using the following equation:

$$q_t = \frac{(C_i - C_t)}{W} \times V \quad (19)$$

where  $C_t$  ( $\text{mg}/\text{L}$ ) is the equilibrium concentration of MB at a certain time ( $t$ ).

## 2.7 Thermodynamic Parameters for MB Adsorption onto Solid Nanoadsorbents

Different thermodynamic parameters as the change of enthalpy ( $\Delta H^\circ$ ), entropy ( $\Delta S^\circ$ ), Gibbs free energy ( $\Delta G^\circ$ ), and equilibrium constant ( $K_a$ ) were evaluated to study the heat of adsorption, spontaneity, and the ability of MB adsorption on the surface of solid adsorbents nanoparticles [33].

Van't Hoff equation is used to calculate  $\Delta H^\circ$  and  $\Delta S^\circ$  from the application of Eq. 20.

$$\ln K_a = \frac{\Delta S^\circ}{R} - \frac{\Delta H^\circ}{RT} \quad (20)$$

$$K_a = \frac{C_s}{C_e} \quad (21)$$

$$\Delta G^\circ = \Delta H^\circ - T \Delta S^\circ \quad (22)$$

where  $C_s$  ( $\text{mg}/\text{g}$ ),  $C_e$  ( $\text{mg}/\text{L}$ ), and  $K_a$  are the mass of surface adsorbed dye, the equilibrium concentration of MB at equilibrium, and distribution coefficient for the adsorption process, respectively.

## 2.8 Methylene Blue Desorption

To test MB desorption from the solid adsorbent, MB was preloaded onto the surface of solid adsorbent by mixing 0.5 g of NC with 100 mL, 750 mg/L of MB solution in 200 mL bottle, shaking for 48 h, followed by filtration, simple washing with distilled water, and drying at 45 °C. Various selected desorption solutions (50 mL) as distilled water, ethanol (97%), butanol (99%), HCl (0.1 mol/L), or HCl: ethanol in different ratios (1:1, 1:2, and 2:1) were added to MB preloaded solid adsorbent (0.1 g). The solution was then agitated for about

24 h at 32 °C. The amount of MB desorbed into the desorption solution was calculated via a UV-Vis spectrophotometer. Desorption efficiency was calculated by the following equation [34].

$$\text{Desorption efficiency}(\%) = \frac{C_d \times V}{q \times W} \times 100 \quad (23)$$

where  $q$  ( $\text{mg}/\text{g}$ ),  $W$  ( $\text{g}$ ),  $V$  ( $\text{L}$ ), and  $C_d$  ( $\text{mg}/\text{L}$ ) are the adsorption capacity of adsorbent, the mass of adsorbent, volume of solution, and MB concentration in aqueous solution after desorption process, respectively.

## 2.9 Degradation of Methylene Blue by Photo-Fenton Process

Photo-Fenton degradation of MB was investigated by using a quartz glass box (20x10x5cm) surrounded by aluminum foil containing 100 mL of 20 mg/L of MB solution, 50 mmol of hydrogen peroxide, and 0.15 g of prepared nanocatalyst with continuous stirring. After different time intervals, 1 mL of the solution was removed to be centrifuged and the residual MB concentration was calculated by UV-Vis spectrophotometer. UV radiation with a wavelength of 254 nm originated from (Philips TUV TL 11W Lamp, USA) was utilized to illuminate the solution mixture (10 cm distance from solution surface) in case of photo-Fenton mechanism. The photo-Fenton process was studied after the determination of optimum application conditions through the heterogeneous Fenton process [20].

Nanomagnetite/potassium carrageenan catalyst reusability was determined after three cycles of the MB photo-Fenton degradation process. The catalyst was filtered, gently washed with distilled water followed by drying at 45 °C to be used in the next cycle.

## 2.10 Kinetic and Thermodynamic Parameters for Methylene Blue Photo-Fenton Degradation

Different kinetic and thermodynamic equations were utilized for investigating the photo-Fenton degradation of MB in the presence of prepared nanocatalysts (NM and NC).

### 2.10.1 Kinetic studies of methylene blue Photo-Fenton degradation

The kinetic study of photo-Fenton degradation of MB was investigated using the following linear equation [35]:

$$\ln \frac{C_o}{C_t} = K_{app} t \quad (24)$$

where  $C_o$  and  $C_t$  ( $\text{mg}/\text{L}$ ) are the initial and residual MB concentrations after a certain time.  $t$  (min) is the irradiation time, and  $K_{app}$  is the apparent first-order rate constant.



## 2.10.2 Thermodynamic Studies of Methylene Blue Photo-Fenton Degradation

Photo-Fenton degradation of MB in the presence of nanocatalysts at different application temperatures enables the calculation of activation energy ( $E_a$ , kJ/mol) using Arrhenius equation, enthalpy change ( $\Delta H^*$ , kJ/mol), entropy change ( $\Delta S^*$ , kJ mol<sup>-1</sup> K<sup>-1</sup>), and Gibbs free energy change ( $\Delta G^*$ , kJ/mol) by applying Eqs. 25–27 [36, 37]:

$$\ln k = \ln A - \frac{E_a}{RT} \quad (25)$$

where  $k$  (min<sup>-1</sup>),  $A$ , and  $E_a$  (kJ/mol) are rate constant, frequency factor constant, and activation energy, respectively.  $R$  is the ideal gas constant and  $T$  is the absolute temperature.

$$\ln \frac{k}{T} = \ln \frac{K_b}{h} + \frac{\Delta S^*}{R} - \frac{\Delta H^*}{RT} \quad (26)$$

$$\Delta G^* = \Delta H^* - T \Delta S^* \quad (27)$$

where  $K_b$  ( $1.3 \times 10^{-23}$  J/K) and  $h$  ( $6.623 \times 10^{-34}$  J sec) are Boltzmann and Plank's constants, respectively.

## 3 Results and Discussion

### 3.1 Characterization of Nanoadsorbents and Photocatalysts

Thermal stability, adsorbed moisture, and unstable organic compounds in the resulting solid samples were determined using thermal analysis from room temperature up to 800 °C. Figure 1a shows the thermal degradation of NM, KC, and NC. The degradation of NM occurs in one stage with weight loss < 4% at 800 °C, indicating its high thermal stability. KC and NC degradation occur in three stages, the first period from 115 to 182 °C shows a weight loss of 5.4 and 7.9% at 115 °C for KC and NC, respectively, due to the evaporation of the surface adsorbed water. At 182 °C, the weight loss of KC and NC are 8.6 and 12.4%, respectively, which may be related to the internal absorbed water molecules into the solid structure. The second step is carried out at 300 °C, with weight loss of 14.5 and 18.7%, for KC and NC which may be related to the degradation of organic molecules, carboxylate groups, and polymer chains destruction. The final stage at 775 °C with weight loss of about 25.1 and 30.2% for KC, and NC, respectively. It is related to the evolution of volatile carbonaceous compounds that originated from the combustion of organic compounds. Thermal stability of NC < KC can be related to the influence of NM on the cross-linkages of KC polymer structure [38, 39].

XRD patterns of NM, KC, and NC are displayed in Fig. 1b. XRD for NM reveals seven distinctive peaks which were located at 2θ degree of 30.3, 35.6, 38.3, 43.5, 53.4, 57.6, and 63.1 ° which are fitted with (220), (311), (222), (400), (422), (511), and (440) diffraction planes and confirming the cubic structure of NM. The prepared NM is crystalline and pure due to the absence of any peaks that cannot be identified [40, 41]. In this study, XRD for KC is exhibited as high crystalline peaks and disappearance of amorphous peak at 2θ degree of 10°–30° as expected and may be related to the crosslinking of K<sup>+</sup> with kappa-carrageenan during the gelation process [42]. Potassium ions change carrageenan structure from single coil to double helix and increases the carrageenan crystallinity [43]. NC peaks are less crystalline than KC which is related to the effect of NM on crosslinking of KC structure during composite formation [44, 45]. Using Debye–Scherrer model (Eq. 28) for the calculation of average crystalline sizes ( $P_s$ , nm) for NM, KC, and NC.

$$P_s(\text{nm}) = \frac{\lambda k}{\beta \cos \theta} \quad (28)$$

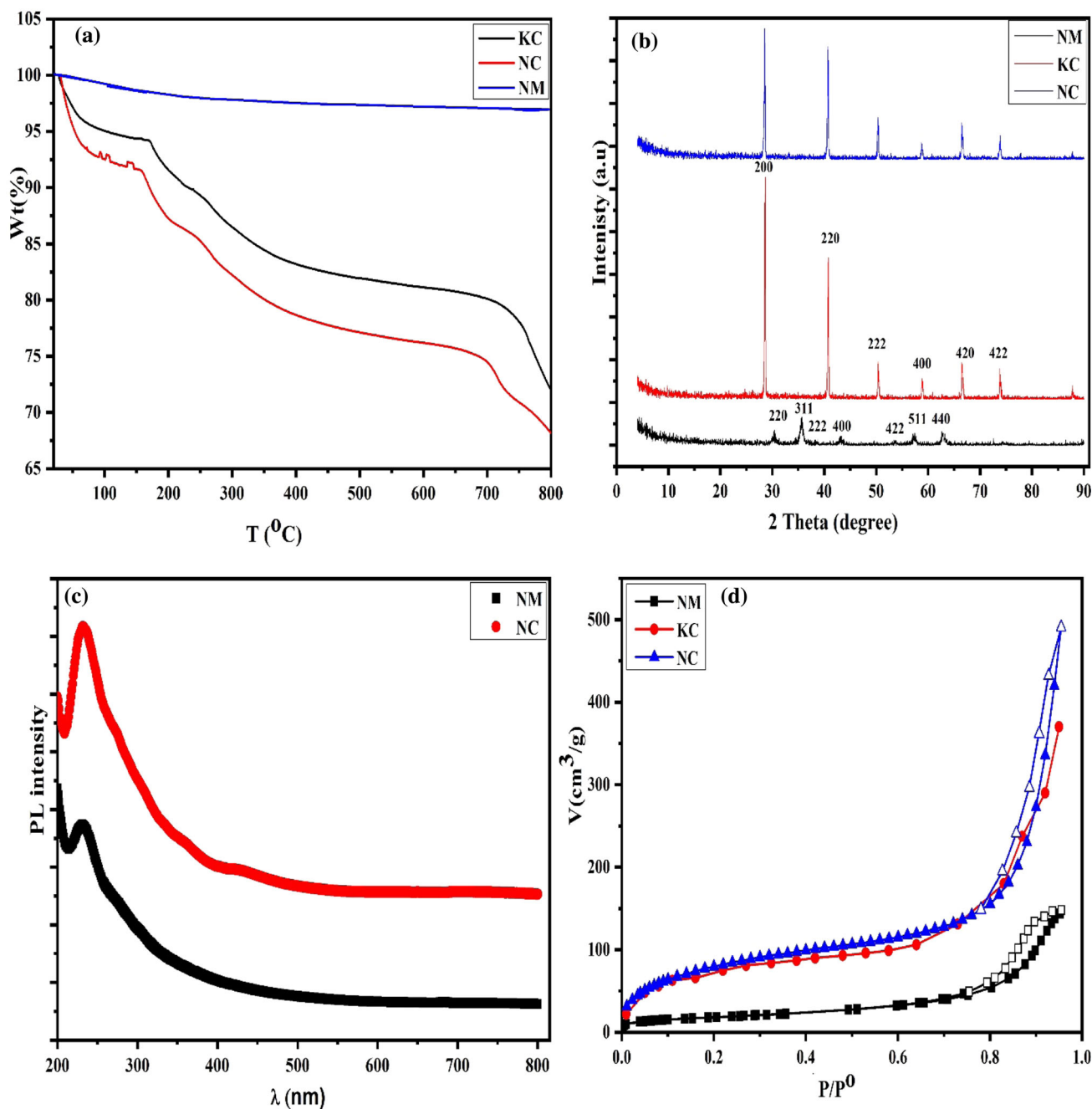
where  $\beta$  represents the full width at half the maximum of peaks,  $k = 0.9$  and  $\lambda$  is the wavelength of X-ray equals 0.15418 nm. The average size of coherent crystallite domains of NM, KC, and NC was calculated using the diffraction lines located at 2θ angles of 62.69, 40.76, and 73.83° were found to be 0.9, 1.8, and 0.7 nm, respectively [46].

Figure 1c shows DRS which is utilized to investigate the optical characteristics of NM and NC by applying the following equation:

$$E_{bg}(\text{eV}) = \frac{1240}{\lambda(\text{nm})} \quad (29)$$

where  $\lambda$  is the semiconductor excitation wavelength, NM and NC have energy band gaps ( $E_{bg}$ ) of 2.90 and 2.53 eV, respectively. Owing to the reduction of the NC band gap, its catalytic effectiveness can be enhanced as a result of the increase in chemical functional groups and surface charges of NC after modification of NM by KC. The bandgap is also affected by the variation of particle size of catalyst nanoparticles [47, 48].

Nitrogen adsorption/desorption isotherms of NM, KC, and NC are shown in Fig. 1d which is mainly used to determine their activity by calculating textual parameters such as pore radius, specific surface area, and total pore volume as displayed in Table 1. According to the classification of IUPAC, adsorption isotherms are typical to type IV while NM and NC with hysteresis loops of H2 type, this type confirm the formation of adsorbed monolayer [49]. The calculated specific surface areas are 96.7, 363.0, and 406.0 m<sup>2</sup>/g, while the total pore volume was found to be 0.22, 0.57, and 0.74 cm<sup>3</sup>/g for NM, KC, and NC, respectively. The observed increase in



**Fig. 1** TGA (a), XRD (b), N<sub>2</sub> adsorption/desorption isotherms (c), and DRS (d) of samples

$V_T$  (cm<sup>3</sup>/g) with specific surface area is due to the increase in porosity and chemical functional groups of polysaccharides (*k*-carrageenan) [47]. The H2 type of hysteresis loop for nanosolid materials may be related to the formation of porous inorganic oxides affecting the connectivity of pores [16]. Pore radius of NM, KC, and NC is 4.55, 3.14, and 3.64 nm, respectively, confirming that all samples are mesoporous. The pore size of NC is less than NM by about 20% owing to the effect of polymer inserted into the structure of NM during composite formation [50, 51].

Figure 2a, b shows SEM images to exhibit the morphological structure of NM and NC, respectively. NM appears as a circle-like morphology with an aggregated rough surface and the agglomeration of NM is due to its magnetic characters. NC shows a more aggregated structure with particle size more than NM and a more porous structure because nanomagnetite is uniformly incorporated into the KC blend [52].

Figure S1 (a, b) represents EDX analysis of NM and NC, respectively. NM contains iron of 94.1 and oxygen of 5.86%,

**Table 1** Textural parameters, point of zero charges, and swelling ratios for NM, KC, and NC solid samples

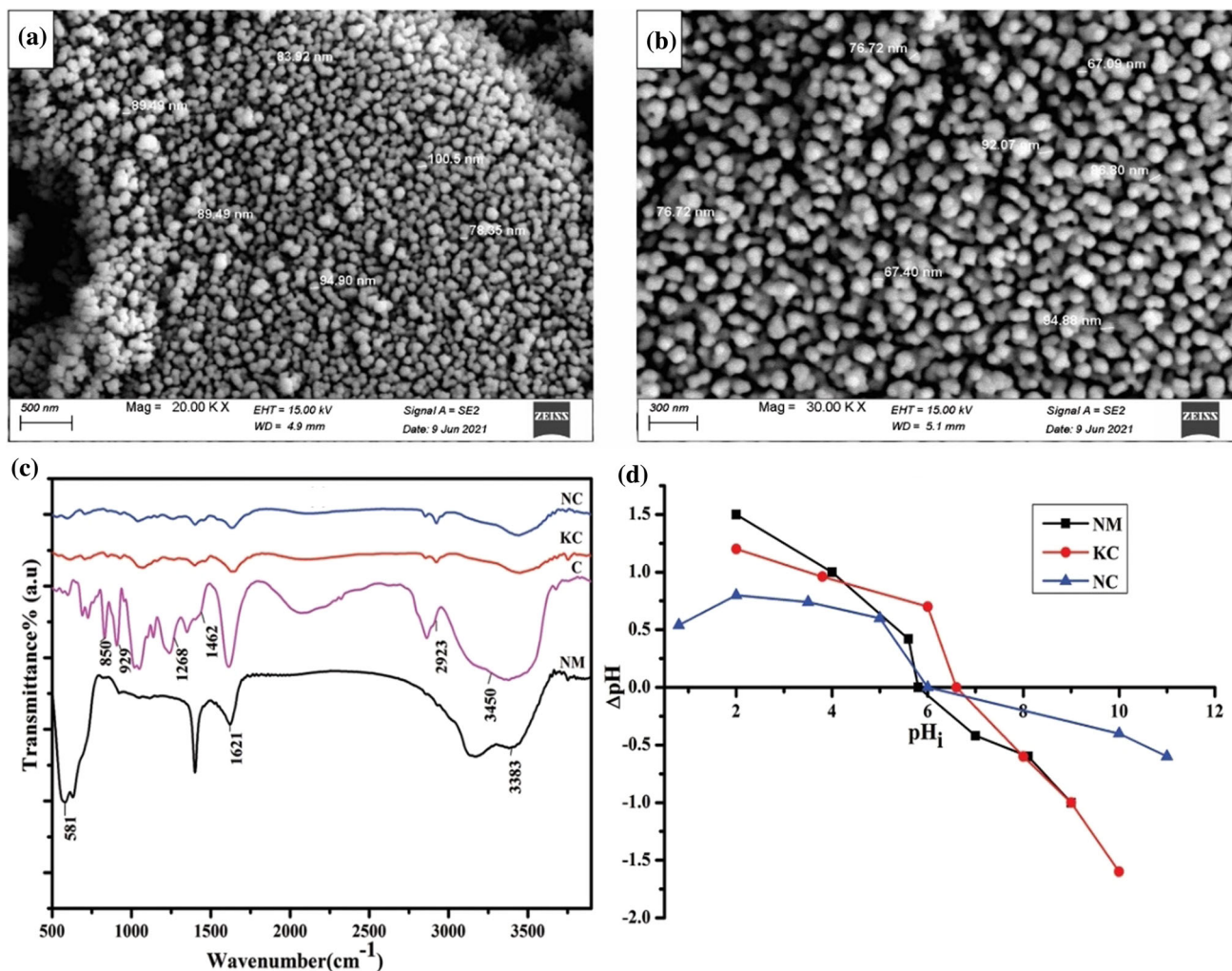
Parameters	NM	KC	NC
$S_{BET}$ (m <sup>2</sup> /g)	96.7	363.0	406.0
$V_T$ (cm <sup>3</sup> /g)	0.22	0.57	0.74
$\bar{r}$ (nm)	4.5502	3.1405	3.6453
pHPZC	5.80	6.60	6.00
SR (%)	0	385	1

$S_{BET}$  is the specific surface area,  $V_T$  is the total pore volume,  $\bar{r}$  is the pore radius, pHPZC is pH of the point of zero charges, and SR %, is the percent of swelling ratio

which confirms its high purity, while NC contains 1.97, 33.1, 40.7, and 24.2% for iron, chloride, potassium, and oxygen, respectively. Figure S1 (c, d) represents TEM micrographs of NM and NC. NM has the appearance of a spherical homogeneous shape with an average particle size of about 5 nm. In the

case of NC composite, it is observed that NM is evenly distributed throughout the KC polymer network with a particle size of about 140 nm [53].

FTIR is used for the identification of surface functional groups for NM, KC, and NC (Fig. 2c). The peak located at 581 cm<sup>-1</sup> is a characteristic peak of NM and is related to (Fe-O) stretching vibration frequency. The band located at 1621 cm<sup>-1</sup> is attributed to bending vibration of (H-O-H) owing to the physisorption of water at the surface of NM, and 3383 cm<sup>-1</sup> is related to OH stretching vibration [49, 54]. For KC, peaks that appeared at 850, 929, and 1072 cm<sup>-1</sup> are related to C-O-S (d-galactose 4-sulfate), 3,6 anhydro d-galactose, and glycosidic linkage, respectively. Absorption peaks at 1268, 1462, and 2923 cm<sup>-1</sup> are attributed to ester sulfate stretching, absorbed water, and C-H-stretching, respectively. Bands located at 1631 and 3450 cm<sup>-1</sup> are also related to absorbed water and OH stretching in KC polymer. As observed in FTIR, kappa-carrageenan (C) has the same peaks of KC with stronger intensities than KC and this is due to the effect of KCl

**Fig. 2** SEM micrographs for NM and NC (a, b), FTIR (c), and pHPZC (d) for samples



on the structure of kappa-carrageenan, which was also confirmed by XRD data. NC peaks appeared at 596, 1041, 1262, 1635, and 2923  $\text{cm}^{-1}$  are attributed to Fe-O, C-O stretching, ester sulfate stretching, absorbed water, and C-H stretching, respectively. Shifts that were occurred in NC peaks compared to NM may be related to the effect of NM on KC structure during the formation of NC composite [26, 38].

The calculation of point of zero charge is an important factor in adsorption from solution at the solid/liquid interfaces. The calculated  $\text{pH}_{\text{PZC}}$  values from Fig. 2d curves are depicted in Table 1 and found to be in the range 5.8–6.6 for all the prepared solid adsorbents [55].

The swelling ratios (SR) for all the prepared solid materials were determined to evaluate the feasibility of solid materials in aqueous applications. Hydrogels such as carrageenan are three-dimensional polymeric networks that swell quickly when they absorb a substantial amount of water or biological fluids and shrink when their external environment changes which affect the adsorption process [56]. The calculated swelling ratios for NM, KC, and NC were found to be zero, 385, and 1% as presented in Table 1. The higher SR for KC (> 3.8 times its original weight) is related to its higher hydrophilicity and that is due to the presence of abundant polar chemical functional groups on its surface. The formation of new NC composite originated from KC and NM is accompanied by a sharp decrease in SR (1%), which may be due to the strong formed chemical bonds in the composite matrix. KC is not preferred as a solid adsorbent due to its higher swelling ratio and solution uptake.

## 3.2 Static Adsorption of Methylene Blue onto the Prepared Solid Adsorbents

### 3.2.1 Effect of Adsorbent Dosage

Nanomagnetite was selected for studying the effect of adsorbent dosage (0.3 to 2.5 g/L) on the removal of MB from an aqueous solution (Fig. 3a). As the adsorbent dosage of NM increases up to 2.0 g/L the removal % is well enhanced due to increasing the number of active sites at the surface of NM with increasing its dosage weight. At dosage more than 2.0 g/L, the removal % of MB nearly has constant values because of the establishment of adsorption equilibrium at a lower concentration of MB even if the presence of more active sites at NM surface. The maximum removal % of MB was selected at 2.0 g/L as adsorbent dosage.

### 3.2.2 Effect of pH

pH is considered as one of the most important factors that affect the adsorption of MB from solution onto the surface of any solid adsorbent. The effect of pH of MB solution was studied at pH range from 2 to 11 using 0.1 g of NM, 50 mL of

100 mg/L MB solution, 30 h as shaking time, and at 15 °C. Figure 3b shows that by increasing the pH range from 2 to 11, the removal percent of NM increases. Considering  $\text{pH}_{\text{PZC}}$  for NM, we observed that at  $\text{pH} < \text{pH}_{\text{PZC}}$ , the surface of NM will be positive leading to the lower adsorption capacity of MB onto the investigated solid adsorbent due to the formation of  $\text{H}_3\text{O}^+$  that easily competes with MB on NM active sites. The surface of NM will acquire a negative charge at  $\text{pH} > \text{pH}_{\text{PZC}}$  which is accompanied by an increase in adsorption capacity via increasing the attraction force between MB and negative active sites of NM surface [2].

### 3.2.3 Effect of Shaking Time and Kinetic Parameters

Different models have been utilized for determining kinetic parameters and rate-determining step for the adsorption process. In this study, adsorption rate is determined by using several kinetic models as PFO, PSO, and Elovich kinetic models for MB adsorption onto NM, KC, and NC after different time intervals up to 48 h, pH6.5, 0.1 g of dosage, 50 mL of 100 mg/L MB, and at 15 °C. The capacities of adsorption of all samples against shaking time are presented in Fig. 3c. The adsorption rate of MB at the beginning up to 10 h sharply increased for all the investigated solid adsorbents, slightly increased from 10 to 25 h, and remains unchanged from 25 to 48 h. At the beginning time, the enhancement of adsorption rate is owing to the presence of many active sites at the surface of all solid adsorbents nanoparticles. In other words as active sites increase, the rate of adsorption also increased [57]. The slowdown and unchanging adsorption rate after 10 and 25 h, respectively, are related to the saturation of surface-active sites with MB ions. PFO, PSO, and Elovich kinetic models are shown in Figure S2a, Fig. 3d, e, respectively, while different kinetic parameters are presented in Table 2. Adsorption of MB is highly fitted by PSO model owing to the small differences between the calculated experimental adsorption capacities ( $q_{\text{ex}}$ , mg/g) and the Langmuir adsorption capacity ( $q_{\text{m}}$ , mg/g) for adsorption in addition to the higher correlation coefficients (0.9999–0.9982) for all the investigated solid adsorbents. Adsorption rate constants ( $k_2$ ,  $\text{g}/\text{mg h}^{-1}$ ) for  $\text{NC} > \text{KC} > \text{NM}$  mean that modification with polysaccharides raises the chemical surface functional groups which are responsible for adsorption. The calculated  $R^2$  values for the adsorption of MB dye by PFO kinetic models are also high (> 0.9661) but the observable large difference between the calculated and experimental adsorption capacities (46.6–75.9%) proves that adsorption doesn't obey PFO kinetic model. Elovich model is perfectly applied for MB adsorption based on the higher calculated correlation coefficients for all solid adsorbents (0.9890–0.9833) [29, 58].

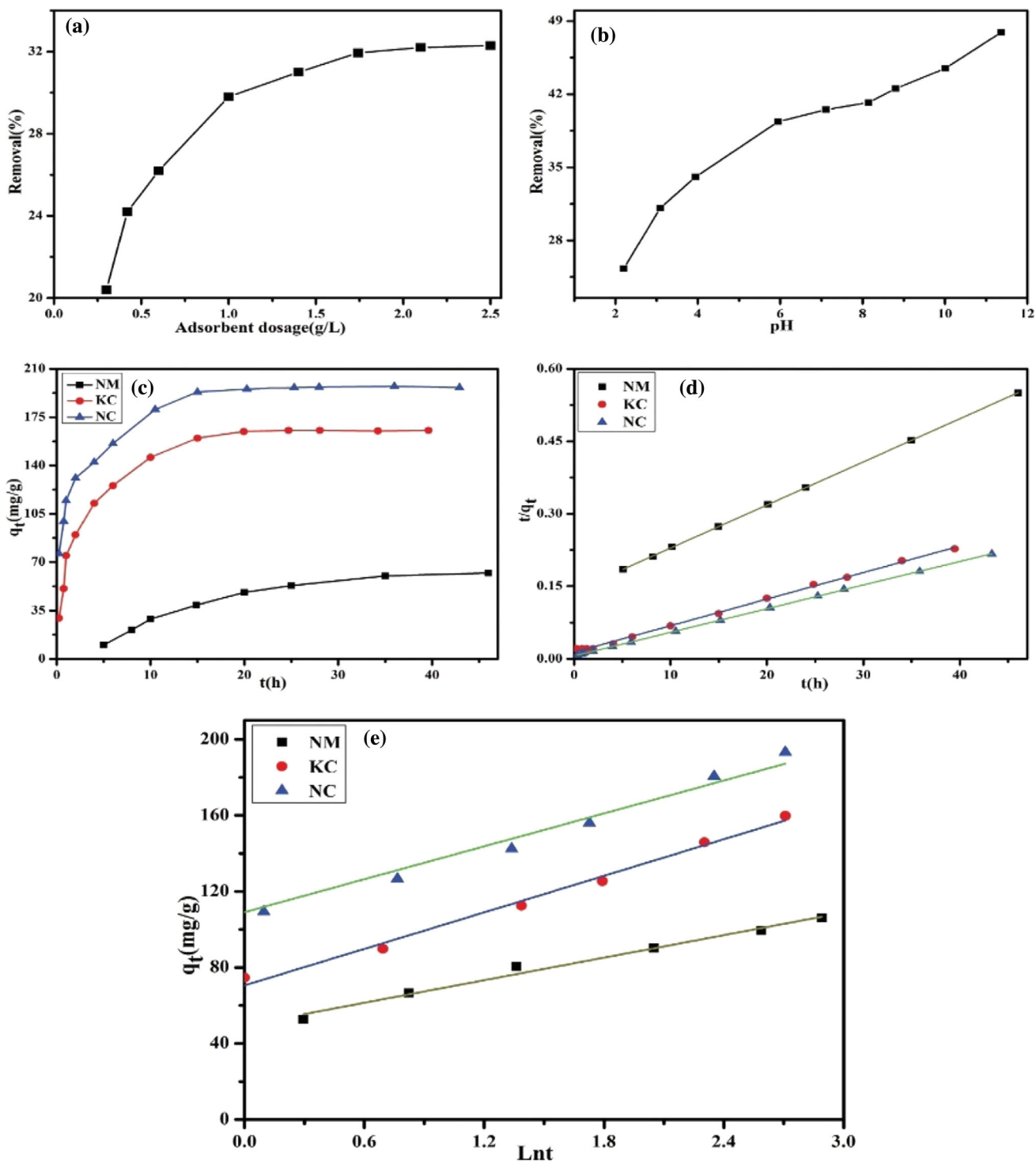


Fig. 3 Effect of dosage (a), pH (b) for NM, shaking time (c), PSO and Elovich (d, e)

**Table 2** Parameters of kinetic models for the adsorption of MB onto the surface of NM, KC, and NC at 15 °C

Samples	PFO				PSO			Elovich		
	$q_m$ (mg/g)	$R^2$	$q_{exp}$ (mg/g)	$k_1$ (h <sup>-1</sup> )	$R^2$	$q_{exp}$ (mg/g)	$k_2 \times 10^{-3}$ (g/mg.h <sup>-1</sup> )	$R^2$	$\alpha$ (mg/g.h <sup>-1</sup> )	$\beta$ (g/mg)
NM	88.03	0.9661	21.2	0.046	0.9999	109.9	0.57	0.9842	241.7	0.0505
KC	168.10	0.9879	89.7	0.066	0.9982	179.4	2.66	0.9890	289.4	0.0312
NC	220.30	0.9792	112.7	0.039	0.9999	210.5	3.81	0.9833	1267.6	0.0347

**Table 3** Parameters of Langmuir, Freundlich, Temkin, and Dubinin–Radushkevich models for MB adsorption onto NM, KC, and NC at 15, 28, 40 °C

Samples	NM			KC			NC		
	15 °C	28 °C	40 °C	15 °C	28 °C	40 °C	15 °C	28 °C	40 °C
<i>Langmuir parameters</i>									
$q_m$ (mg/g)	88.03	97.28	102.88	168.10	207.00	222.70	220.30	314.50	374.50
$K_L$ (L/mg)	0.0466	0.0901	0.1359	0.3388	0.6474	0.5719	0.0471	0.0295	0.0279
$R_L$	0.1767	0.0999	0.0689	0.0286	0.0152	0.0172	0.1754	0.2533	0.2641
$R^2$	0.9973	0.9955	0.9991	0.9915	0.9978	0.9962	0.9999	0.9973	0.9771
<i>Freundlich parameters</i>									
$1/n$	0.5195	0.3571	0.2624	0.3951	0.1554	0.1646	0.1850	0.2610	0.2585
$K_F$ (L/mg)	8.069	20.18	32.70	34.02	111.6	117.2	75.22	67.93	78.41
$R^2$	0.9855	0.9910	0.9974	0.9766	0.9822	0.9858	0.9846	0.9946	0.9936
<i>Temkin parameters</i>									
$b_T$ (J/mol)	103.90	130.90	137.50	84.36	102.60	101.40	57.47	45.34	35.75
$K_T$ (L/g)	0.288	1.226	2.359	1.914	3.655	4.950	0.895	2.390	3.700
$R^2$	0.9948	0.9956	0.9972	0.9788	0.9922	0.9896	0.9967	0.9982	0.9986
<i>Dubinin–Radushkevich parameters</i>									
$q_{DR}$ (mg/g)	71.73	79.54	89.28	141.7	184.7	210.9	219.78	321.5	337.0
$E_{DR}$ (kJ/mol)	0.1059	0.2465	0.2852	0.3517	0.4312	0.3408	0.2433	0.1832	0.2126
$R^2$	0.9893	0.9777	0.9814	0.9980	0.9854	0.9871	0.9965	0.9994	0.9993

**3.2.4 Effect of Initial Concentration of Methylene Blue Dye**

Adsorption isotherms for the adsorption of MB onto the surface of NM, KC, and NC using 0.1g dosage, initial concentration varying from (10–600 mg/L), and after 24 h for shaking time at 15, 28, and 40 °C are displayed in Fig. 4a. Figure 4a indicates that the adsorption of MB at lower initial concentration is very high due to the higher ratio of the number of MB ions to active sites for all the adsorbents, while at the end period of isotherms, the adsorption slowdowns with decreasing the previous ratio. Figure S2 (b-d) and Figure S3 (a-c) depict the adsorption model of Langmuir and Freundlich on the surface of NM, KC, and NC, respectively, while calculated parameters are illustrated in Table 3.

Langmuir isotherm model is well applied according to the high values of  $R^2$  at different temperatures for all prepared solid adsorbent samples. Upon analysis of data in Table

3 (i) maximum Langmuir adsorption capacities ( $q_m$ , mg/g) for NM, KC, and NC are 102.88, 222.70, and 374.50 mg/g, respectively, at 40 °C which may be related to the specific surface area, total pore volume, and the presence of chemical functional groups for NC>KC>NM as reported in Table 1 and FTIR curves. The previous results prove the effectiveness of the NC composite that was formed between NM and KC in the adsorption process. (ii) For all solid adsorbents, as temperature increases the adsorption capacities also increase which means endothermic nature for the adsorption process. (iii) Dimensionless separation factors ( $R_L$ ) are ranged between 0.0152 and 0.2641 indicating a favorable adsorption process. (iv) Correlation coefficient values calculated for the Freundlich model (0.9974–0.9766) are less than that calculated for Langmuir (0.9999–0.9771) for all the studied solid samples which prove the well-fitting of the

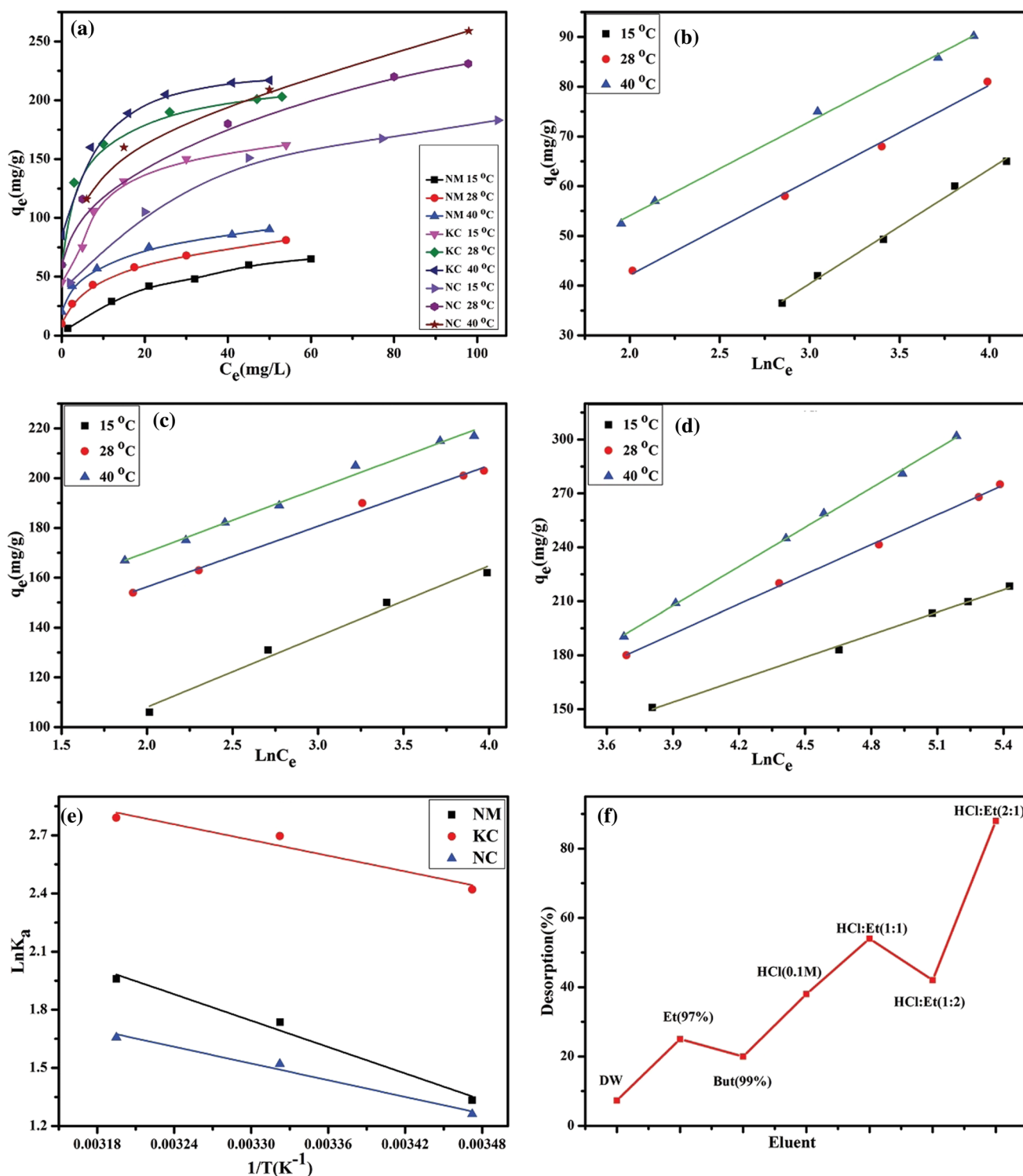


**Fig. 4** Adsorption isotherms (a), Temkin (b–d), Van't Hoff (e) plots, and NC desorption studies (f)

Langmuir equation compared with Freundlich. (v) The calculated Freundlich  $1/n$  values are less than unity and ranged between 0.1554 and 0.5195 for adsorption of MB by all the prepared solid adsorbents and proved the normal Langmuir isotherm [59]. Figure 4b–d shows the Temkin adsorption

model onto NM, KC, and NC while Temkin parameters are listed in Table 3.  $R^2$  values for all solid samples are located in the range 0.9788–0.9986 at all the applied adsorption temperatures which confirm the perfectly fitted Temkin model. Binding constants at equilibrium for modified sample KC are

more than NM and NC and indicating the stronger binding force between MB dye and KC. Also,  $K_T$  values increased with temperature for all the solid samples which proves the endothermic adsorption process. Temkin  $b_T$  values for NM, KC, and NC at different application temperatures lie between 35.75 and 137.50 J/mol ( $b_T < 8000$  J/mol) which represent physical adsorption of MB on solid adsorbents [60].

Dubinin–Radushkevich model for adsorption of MB onto NM, KC, and NC is shown in Figure S3 (d-f) and the calculated DR parameters are listed in Table 3. The calculated  $R^2$  values for NM, KC, and NC at different temperatures  $> 0.9777$ . The difference between maximum adsorption capacities calculated from DR model ( $q_{DR}$ , mg/g) and that calculated from Langmuir models ( $q_m$ , mg/g) ranged between 0.2 and 15.5% for all the investigated samples at different applied temperatures. The previous two observations prove that the adsorption of MB is perfectly fitted by DR isotherm model. The calculated mean free energy ( $E_{DR}$ , kJ/mol) that determines the adsorption nature of MB dye onto the surface of all nanosolid adsorbents is less than 8.0 kJ/mol confirming the physical adsorption process [61]. All the previous results indicate that the adsorption of MB data is perfectly fitted with Langmuir, Temkin, and Dubinin–Radushkevich. Langmuir adsorption isotherms.

### 3.2.5 Effect of Temperature and Thermodynamic Parameters

Adsorption of MB on the surface of NM, KC, and NC was investigated at different temperatures (15, 28, and 40 °C) to determine different thermodynamic parameters as shown in Van't Hoff plots (Fig. 4e). Upon inspection of thermodynamic parameters in Table 4 (i) the higher correlation coefficients ( $R^2 > 0.9237$ ) for Fig. 4e indicate the good linear fitting of Van't Hoff plots. (ii) The positive values of  $\Delta S^\circ$  for all the samples confirm the increase in MB randomness at the solid surface during the adsorption process. (iii)  $\Delta H^\circ$  ranged between 11.23 and 18.85 kJ/mol and indicates endothermic adsorption process which proves the increase in the maximum adsorption capacities for all the solid samples (NM, KC, and NC) with temperature. The values of  $\Delta H^\circ$  (less than 25 kJ/mol) illustrate that Van der Waals interactions are the dominant confirming physical adsorption process. (iv)  $\Delta G^\circ$  values (3.050–7.331 kJ/mol) are negative for all samples which indicate the spontaneous and favorable adsorption process [62].

### 3.3 Desorption Studies

Desorption of MB from the surface of NC was studied using different desorbing solutions as indicated in Fig. 4f. The desorption efficiency of HCl: ethanol (2:1), HCl: ethanol (1:1), HCl: ethanol (1:2), HCl (0.1 M), ethanol (97%), butanol

(99%), and distilled water were found to be 91, 54, 42, 38, 25, 20, and 7.3%, respectively. HCl: ethanol (2:1) is the most effective desorbing solution for pre-adsorbed methylene blue [63].

### 3.4 Methylene Blue Degradation Using Heterogeneous Fenton Process

Degradation of MB by heterogeneous Fenton process is studied by different parameters such as catalyst dosage, the concentration of hydrogen peroxide, MB initial concentration, the effect of pH, effect of temperature, and UV illumination.

#### 3.4.1 Effect of Catalyst Dosage

The effect of NM dosage as selected solid nanocatalyst on the degradation of MB against time by varying dosage from 0.8 to 2.0 g/L using 50 mmol of  $H_2O_2$ , 10 mg/L of MB as initial concentration, pH 3, and at 18 °C is shown in Fig. 5a. It is obvious that with increasing NM dosage up to 1.5 g/L dosage, the degradation of MB increases and starts to decrease at NM dosage more than 1.5 g/L. Enhancing the degradation of MB with increasing dosage is related to the increase in the number of active sites with increasing NM dosage mass, and the increase in the number of ferrous ions that react with hydrogen peroxide to produce  $\cdot OH$  (Eq.1) which is responsible for MB degradation. Degradation of MB decreases at NM dosage more than 1.5 g/L is due to the effect of scavenging of ferrous ion on hydroxyl radical as reported by Eq.30 [64]. 1.5 g/L has been selected as the optimum catalyst dosage during Fenton degradation of MB.

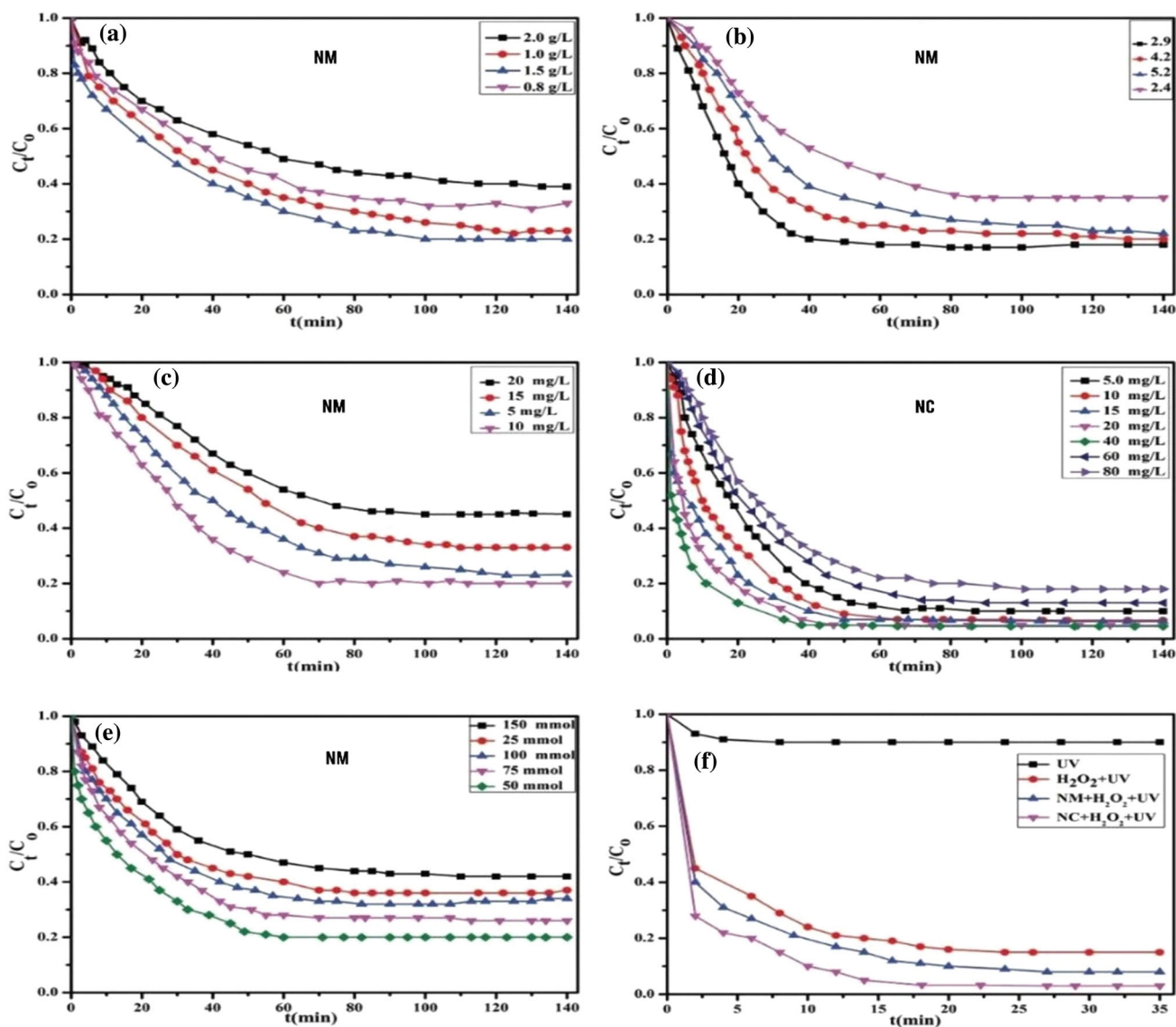


#### 3.4.2 Effect of pH on Methylene Blue Degradation

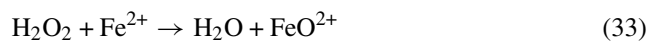
The effect of pH on MB degradation was studied by varying pH ranges (2.4–5.2), using 1.5 g/L of NM as catalyst dosage, 10 mg/L of MB, 50 mmol of hydrogen peroxide concentration at 18 °C (Fig. 5b). After 90 min, the degradation percentage of MB was found to be 65, 83, 78, and 74% at pH 2.4, 2.9, 4.2, and 5.2, respectively. Degradation of MB increases with increasing pH till pH 2.9 and further increasing in pH values are accompanied by decreasing in MB degradation efficiency. Lower degradation MB at lower pH values is due to the stability of  $H_2O_2$  through the formation of stable  $H_3O_2^+$  (oxonium ion) by protonation of hydrogen peroxide with  $H^+$ , the conversion of hydroxyl radicals to water molecules, and the formation of  $FeO^{2+}$  as inactive ion as

**Table 4** Thermodynamic parameters for the adsorption of MB onto NM, KC, and NC

Solid samples	$R^2$	$\Delta H^\circ$ (kJ/mol)	$\Delta S^\circ$ (kJ mol <sup>-1</sup> K <sup>-1</sup> )	$-\Delta G^\circ$ (kJ/mol)		
NM	0.9858	11.23	0.0593	15 °C	28 °C	40 °C
				5.850	6.619	7.331
				KC	0.9237	11.90
NC	0.9810	18.85	0.0767	3.239	4.236	5.157

**Fig. 5** Effect of dosage (a), pH (b), initial concentration (c, d), [H<sub>2</sub>O<sub>2</sub>] (e), and Photo-Fenton studies (f)

shown in Eqs. 31–33, respectively [65].



At higher values of pH, the efficiency of MB degradation decreases due to the formation of water and oxygen by hydrogen peroxide decomposition and the formation of iron hydroxide instead of  $\cdot\text{OH}$  formation by ferrous ion [66, 67].

The previous result proves that the acidity of solution around pH3 exhibits the maximum degradation efficiency.

### 3.4.3 Effect of Initial Methylene Blue Concentration

Figure 5c, d represents the effect of MB initial concentration by varying concentration from 5–20 and 5–80 mg/L in case of NM and NC, respectively, 1.5 g/L as catalyst dosage, pH3, 50 mmol of H<sub>2</sub>O<sub>2</sub> concentration at 18 °C. In the presence of NM and after 120 min, the degradation of MB reached 77, 80, 67, and 55% using MB concentration of 5, 10, 15, and 20 mg/L while in the case of NC and after 90 min, the degradation efficiency reached 90, 93, 94, 95, 96, 86, 80% in the presence of 5, 10, 15, 20, 40, 60, and 80 mg/L as MB initial concentration. The previous data show that modification of NM with potassium carrageenan to form new composite (NC) beads raises the extent of MB degradation which may be related to the distribution of ferrous ions on the surface of composite, the good fixation of MB ions onto the composite surface, and the reduction in the required activation energy for the degradation process. At the initial periods of increasing initial concentration of MB, we observed that the degradation efficiency using the heterogeneous Fenton process also increases and is related to the increase in collisions between the oxidizing species and MB molecules. The excessive increase in initial concentration > 10 and 40 mg/L in the case of NM and NC, respectively, is accompanied by a reduction in degradation ratios and that is related to the increase in the ratio of MB molecules/ oxidizing species [68].

### 3.4.4 Effect of hydrogen peroxide concentration

Hydrogen peroxide is considered as the main source of ·OH in the Fenton process for MB degradation. Figure 5e shows the effect of hydrogen peroxide concentration from 25 to 150 mmol, 1.5 g/L as NM dosage, 10 mg/L of MB as initial concentration, pH3, and at 18 °C. Degradation of MB after 120 min reached about 64, 80, 74, 67, and 58% in the presence of 25, 50, 75, 100, and 150 mmol of H<sub>2</sub>O<sub>2</sub>, respectively. It is observed that the degradation increases with hydrogen peroxide concentration up to 50 mmol and starts to decrease dramatically till reaches 58% in the presence of 150 mmol H<sub>2</sub>O<sub>2</sub>. The increase in efficiencies of degradation at the beginning is due to the increase in ·OH as oxidizing species while the decrease at higher concentrations of hydrogen peroxide is related to the scavenging of ·OH and the formation of less active oxidants as reported in Eqs. 34, 35 which is accompanied by deviation in the mechanism of heterogeneous Fenton process [69]. The optimum selected concentration of hydrogen peroxide is 50 mmol.

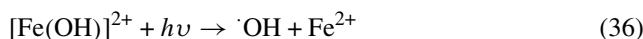


## 3.5 Methylene Blue Degradation by Photo-Fenton Process

### 3.5.1 Effect of UV Illumination on the Degradation of MB

Four experiments were carried out for studying MB photo-Fenton degradation namely (i) 20 mg/L of MB solution was illuminated with UV light (photolysis, 254 nm). (ii) 20 mg/L of MB solution, 50 mmol of H<sub>2</sub>O<sub>2</sub>, and UV radiation. (iii) 0.15 g of NM catalyst with 20 mg/L of MB solution, 50 mmol of H<sub>2</sub>O<sub>2</sub> under UV radiation. (iv) 20 mg/L of MB solution, 50 mmol of H<sub>2</sub>O<sub>2</sub>, and 0.15 g of NC catalyst under UV illumination, and all experiments were carried out at pH3 and 18 °C. For all the experiments, after different time intervals, 1 mL of MB solution was removed, centrifuged, and the residual concentration of MB was determined by UV–vis spectrophotometer. Photo-Fenton and photolysis degradation of MB is shown in Fig. 5f. After 20 min, the degradation of MB was calculated to be 10.0, 81.2, 89.1, and 96.9% for photolysis in the absence and presence of H<sub>2</sub>O<sub>2</sub>, and photo-Fenton process in the presence of NM or NC, respectively. The incorporation of H<sub>2</sub>O<sub>2</sub> during photolysis in the second experiment raises the efficiency of degradation from 10.0 to 81.2% due to the release of ·OH which acts as strong oxidizing species for MB molecules [20].

Photo-Fenton experiment using NC as solid nanocatalyst exhibited higher degradation efficiency than NM which may be related to the higher porosity, specific surface area, the abundance of polar chemical functional groups created from carrageenan, and the well surface distribution of ferrous ion in the case of NC solid matrix [35]. Comparing the degradation percentage in the presence of NM or NC after 20 min of application in the case of Fenton and photo-Fenton process, we observe the feasibility of photo-Fenton by about 2.4 and 1.6 times more than Fenton process for NM and NC, respectively. As a general, the increase in the degradation efficiency in the photo-Fenton process is related to the production of ·OH due to the effect of radiation on H<sub>2</sub>O<sub>2</sub> and the reduction of ferric ions into active ferrous ions at the applied pH value as presented in the following equations [70]:



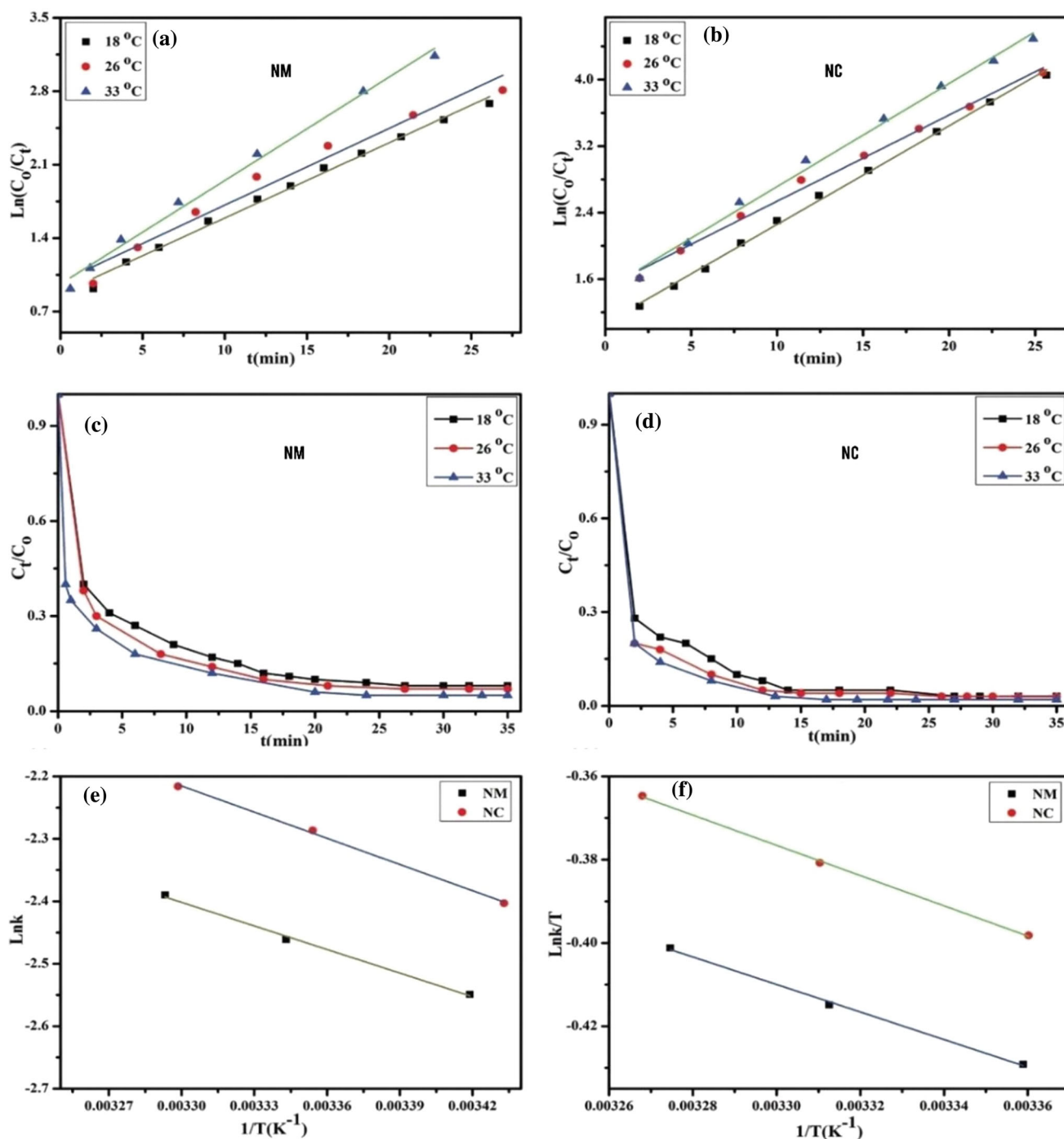


**Fig. 6** Kinetic studies (a, b), effect of temperatures (c, d), Arrhenius (e), and Boltzmann plots (f) for Photo-Fenton

### 3.5.2 Kinetic study of Photo-Fenton Process for Methylene Blue Degradation

Kinetic parameters of MB degradation were determined by using Eq. 24 via plotting  $\text{Ln } C_0/C_t$  against time ( $t$ , min) at 18, 26, and 33 °C as shown in Fig. 6 a, b for NM and NC, respectively, while the calculated parameters are displayed in Table 5. The values of  $R^2$  for NM and NC catalysts are more

than 0.9650, indicating that the photo-Fenton process for both catalysts follows PFO kinetic model. At all the applied temperatures, the measured  $K_{\text{app}}$  (min<sup>-1</sup>) for NC is more than that calculated for NM and related to the higher activity of NC compared with NM. The calculated  $K_{\text{app}}$  increases with temperature for the two catalysts and is due to the increase in the rate of reaction with temperature [71].





**Table 5** Kinetic and thermodynamic studies of Photo-Fenton degradation of MB in the presence of NM and NC at 18, 26, 33 °C

Samples	NM			NC		
	18 °C	26 °C	33 °C	18 °C	26 °C	33 °C
<i>Kinetic parameters</i>						
$K_{app}$ (min <sup>-1</sup> )	0.072	0.073	0.099	0.102	0.112	0.124
$R^2$	0.9930	0.9650	0.9918	0.9979	0.9936	0.9936
<i>Thermodynamic parameters</i>						
$E_a$ (kJ/mol)		10.47			11.61	
$A$		5.773			10.94	
$R^2$		0.9933			0.9966	
$\Delta S^*$ (kJ mol <sup>-1</sup> K <sup>-1</sup> )		- 0.191			- 0.190	
$\Delta H^*$ (kJ/mol)		2.75			3.02	
$R^2$		0.9959			0.9989	
$\Delta G^*$ (kJ/mol)	58.33	59.86	61.19	58.31	59.83	61.16

### 3.5.3 Effect of Temperature on Methylene Blue Degradation by Photo-Fenton Process

The effect of temperature on MB degradation by the photo-Fenton process is represented in Fig. 6c, d for NM and NC catalysts using 0.15 gram as catalysts dosage, pH3, 20 mg/L of MB solution, 50 mmol of hydrogen peroxide at 18, 26, and 33 °C. It is noticed that with increasing temperature, the degradation of MB increases, and that is related to the increase in the number of ·OH as a result of enhancing the rate of reaction between catalyst and hydrogen peroxide which also revealed the endothermic nature of the degradation process [72]. The photo-Fenton activation energies and thermodynamic parameters for MB degradation in presence of NM or NC catalysts were calculated by applying Eqs. 25–27 as shown in Fig. 6e, f while the calculated data are collected in Table 5. Data in Table 5 reveal (i) the good application of Eqs. 25, 26 were confirmed by higher correlation coefficients for both models (> 0.9933). (ii) Photo-Fenton degradation of MB in the presence of prepared nanocatalysts with a physical nature is based on the calculated values of activation energy which is lower than 20 kJ/mol [71]. (iii) The positive values of  $\Delta H^*$  indicate that photo-Fenton degradation of MB is endothermic. (iv) The change in entropy for the process was calculated to be negative 0.191 and 0.190 in the presence of NM and NC, respectively, and that is related to the decrease in the randomness of MB at the surface of catalysts with an irreversible tendency for the process. (v) The change in free energy is positive and proves that the degradation process is nonspontaneous and requires external energy such as radiation and/or heat [36, 37].

### 3.5.4 Catalyst Reusability

Reusability of NC as selected nanocatalyst for MB degradation using the photo-Fenton technique was investigated after 3 cycles of applications as shown in Figure S4. After three cycles, NC suffers from a decrease in catalytic activity by about 9.8%, which may be related to the loss of some active sites, decrease in specific surface area, and porosity due to the coagulation of nanocatalyst particles [16].

### 3.6 Comparison Between NC and Other Adsorbents and Catalysts

In the present study, NC was compared with other reported solid materials for adsorption and photo-Fenton catalytic degradation of MB as indicated in Table S5 [2, 5, 73–79]. Based on data reported in the table it has been concluded that NC is a promising solid nanomaterial for adsorption and photo-Fenton catalytic degradation of methylene blue dye.

### 3.7 Conclusion

Bio-composite beads containing polysaccharides such as potassium carrageenan with unique properties including surface heterogeneity, thermal stability, lower swelling ratio, undetectable water solubility, higher specific surface area, mesoporosity, and the presence of abundant oxygen-containing chemical functional groups. The prepared nanomagnetite/potassium carrageenan composite beads (NC) showed desirable properties including textural, thermal, and chemical characters which encourage us to compare between its adsorption and photo-Fenton degradation of MB dye. NC showed a Langmuir adsorption capacity of 220.3 mg/g at 15 °C and increased with the temperature reaching 374.5



mg/g at 40 °C after 24 h. Adsorption of MB onto all the prepared solid nanomaterials is well fitted by Langmuir, Temkin, and Dubinin–Radushkevich, adsorption isotherms. Kinetic studies prove the good linearity and applications of PSO and Elovich models. Thermodynamic parameters confirm the endothermic and spontaneous adsorption process. The solution containing HCl: ethanol (2:1) plays a very important role in the desorption of MB from the solid surface by about 91% of the pre-adsorbed dye. Photo-Fenton degradation of MB dye (20 mg/L) is a very fast process where 96.9% of the dye completely degrades after 20 min. Comparative studies between adsorption and photo-Fenton degradation process conclude that the photo-Fenton technique is the best choice at lower dye concentration (<40 mg/L) but static adsorption procedures are the best one at higher dye concentration. We believe that a combination between adsorption and photo-Fenton techniques for the removal of MB will cover both lower and higher concentrations of that pollutants. As a general, nanomagnetite/potassium carrageenan bio-composite beads are promising solid materials for adsorption and photo-Fenton applications.

**Supplementary Information** The online version contains supplementary material available at <https://doi.org/10.1007/s13369-022-07075-y>.

**Funding** Open access funding provided by The Science, Technology & Innovation Funding Authority (STDF) in cooperation with The Egyptian Knowledge Bank (EKB).

## Declarations

**Conflict of interest** The authors declare that they have no conflict of interest.

**Open Access** This article is licensed under a Creative Commons Attribution 4.0 International License, which permits use, sharing, adaptation, distribution and reproduction in any medium or format, as long as you give appropriate credit to the original author(s) and the source, provide a link to the Creative Commons licence, and indicate if changes were made. The images or other third party material in this article are included in the article's Creative Commons licence, unless indicated otherwise in a credit line to the material. If material is not included in the article's Creative Commons licence and your intended use is not permitted by statutory regulation or exceeds the permitted use, you will need to obtain permission directly from the copyright holder. To view a copy of this licence, visit <http://creativecommons.org/licenses/by/4.0/>.

## References

- Baig, N.; Ihsanullah, S.M.; Saleh, T.A.: Graphene-based adsorbents for the removal of toxic organic pollutants: a review. *J. Environ. Manag.* **244**, 370–382 (2019). <https://doi.org/10.1016/J.JENVMAN.2019.05.047>
- Mantasha, I.; Saleh, H.A.M.; Qasem, K.M.A.; Shahid, M.; Mehtab, M.; Ahmad, M.: Efficient and selective adsorption and separation of methylene blue (MB) from mixture of dyes in aqueous environment employing a Cu(II) based metal organic framework. *Inorganica Chim. Acta.* **511**, 119787 (2020). <https://doi.org/10.1016/J.ICA.2020.119787>
- Mittal, H.; Babu, R.; Dabbawala, A.A.; Stephen, S.; Alhassan, S.M.: Zeolite-Y incorporated karaya gum hydrogel composites for highly effective removal of cationic dyes. *Colloids Surfaces A Physicochem. Eng. Asp.* **586**, 124161 (2020). <https://doi.org/10.1016/j.colsurfa.2019.124161>
- Mashkoor, F.; Nasar, A.: Magsorbents: potential candidates in wastewater treatment technology—a review on the removal of methylene blue dye. *J. Magn. Magn. Mater.* **500**, 166408 (2020). <https://doi.org/10.1016/J.JMMM.2020.166408>
- Jabli, M.; Almalki, S.G.; Agougui, H.: An insight into methylene blue adsorption characteristics onto functionalized alginate bio-polymer gel beads with  $\lambda$ -carrageenan-calcium phosphate, carboxymethyl cellulose, and celite 545. *Int. J. Biol. Macromol.* **156**, 1091–1103 (2020). <https://doi.org/10.1016/J.IJBIOMAC.2019.11.140>
- Thabede, P.M.; Shooto, N.D.; Naidoo, E.B.: Removal of methylene blue dye and lead ions from aqueous solution using activated carbon from black cumin seeds. *South African J. Chem. Eng.* **33**, 39–50 (2020). <https://doi.org/10.1016/j.sajce.2020.04.002>
- Mittal, H.; Babu, R.; Alhassan, S.M.: Utilization of gum xanthan based superporous hydrogels for the effective removal of methyl violet from aqueous solution. *Int. J. Biol. Macromol.* **143**, 413–423 (2020). <https://doi.org/10.1016/j.ijbiomac.2019.11.008>
- Nwanji, O.L.; Omorogie, M.O.; Olowoyo, J.O.; Babalola, J.O.: Remediation of industrial dye by Fenton-activated biogenic waste. *Surfaces and Interfaces.* **20**, 100555 (2020). <https://doi.org/10.1016/J.SURFIN.2020.100555>
- Saghi, M.H.; Qasemi, M.; Alidadi, H.; Alahabadi, A.; Rastegar, A.; Kowsari, M.H.; Shams, M.; Aziznezhad, M.; Goharshadi, E.K.; Barczak, M.; Anastopoulos, I.; Giannakoudakis, D.A.: Vanadium oxide nanoparticles for methylene blue water remediation: exploring the effect of physicochemical parameters by process modeling. *J. Mol. Liq.* **318**, 114046 (2020). <https://doi.org/10.1016/J.MOLLIQ.2020.114046>
- Sebeia, N.; Jabli, M.; Ghith, A.; El Ghoul, Y.; Alminderej, F.M.: Populus tremula, Nerium oleander and *Pergularia tomentosa* seed fibers as sources of cellulose and lignin for the bio-sorption of methylene blue. *Int. J. Biol. Macromol.* **121**, 655–665 (2019). <https://doi.org/10.1016/J.IJBIOMAC.2018.10.070>
- Mittal, H.; Al Alili, A.; Alhassan, S.M.: High efficiency removal of methylene blue dye using  $\kappa$ -carrageenan-poly(acrylamide-co-methacrylic acid)/AQSOA-Z05 zeolite hydrogel composites. *Cellulose* **27**, 8269–8285 (2020). <https://doi.org/10.1007/s10570-020-03365-6>
- Manojlović, D.; Lelek, K.; Roglić, G.; Zherebtsov, D.; Avdin, V.; Buskina, K.; Sakthidharan, C.; Sapozhnikov, S.; Samodurova, M.; Zakirov, R.; Stanković, D.M.: Efficiency of homely synthesized magnetite: carbon composite anode toward decolorization of reactive textile dyes. *Int. J. Environ. Sci. Technol.* **17**, 2455–2462 (2020). <https://doi.org/10.1007/s13762-020-02654-8>
- Anjum, M.; Miandad, R.; Waqas, M.; Gehany, F.; Barakat, M.A.: Remediation of wastewater using various nano-materials. *Arab. J. Chem.* **12**, 4897–4919 (2019). <https://doi.org/10.1016/J.ARABJC.2016.10.004>
- Nyankson, E.; Kumar, R.V.: Removal of water-soluble dyes and pharmaceutical wastes by combining the photocatalytic properties of Ag<sub>3</sub>PO<sub>4</sub> with the adsorption properties of halloysite nanotubes. *Mater. Today Adv.* **4**, 100025 (2019). <https://doi.org/10.1016/J.MTADV.2019.100025>
- Bello, M.M.; Abdul Raman, A.A.; Asghar, A.: A review on approaches for addressing the limitations of Fenton oxidation for



- recalcitrant wastewater treatment. *Process Saf. Environ. Prot.* **126**, 119–140 (2019). <https://doi.org/10.1016/J.PSEP.2019.03.028>
16. Bulánek, R.; Hrdina, R.; Hassan, A.F.: Preparation of polyvinylpyrrolidone modified nanomagnetite for degradation of nicotine by heterogeneous Fenton process. *J. Environ. Chem. Eng.* **7**, 102988 (2019). <https://doi.org/10.1016/j.jece.2019.102988>
  17. Ren, H.; Jin, X.; Li, C.; Li, T.; Liu, Y.; Zhou, R.: Rosmarinic acid enhanced Fe(III)-mediated Fenton oxidation removal of organic pollutants at near neutral pH. *Sci. Total Environ.* **736**, 139528 (2020). <https://doi.org/10.1016/J.SCITOTENV.2020.139528>
  18. Luo, H.; Zeng, Y.; He, D.; Pan, X.: Application of iron-based materials in heterogeneous advanced oxidation processes for wastewater treatment: a review. *Chem. Eng. J.* **407**, 127191 (2021). <https://doi.org/10.1016/J.CEJ.2020.127191>
  19. Cetinkaya, S.G.; Morcali, M.H.; Akarsu, S.; Ziba, C.A.; Dolaz, M.: Comparison of classic Fenton with ultrasound Fenton processes on industrial textile wastewater. *Sustain. Environ. Res.* **28**, 165–170 (2018). <https://doi.org/10.1016/J.SERJ.2018.02.001>
  20. Thabet, R.H.; Tony, M.A.; Elsherbiny, S.A.; Ali, I.A.; Fouad, M.K.: Catalytic oxidation over nanostructured heterogeneous process as an effective tool for environmental remediation. *IOP Conf. Ser. Mater. Sci. Eng.* (2020). <https://doi.org/10.1088/1757-899X/975/1/012004>
  21. Bekhit, F.; Farag, S.; Attia, A.M.: Decolorization and degradation of the Azo dye by bacterial cells coated with magnetic iron oxide nanoparticles. *Environ. Nanotechnol. Monit. Manag.* **14**, 100376 (2020). <https://doi.org/10.1016/J.ENMM.2020.100376>
  22. Saleh, R.; Taufik, A.: Photo-Fenton degradation of methylene blue in the presence of Au-Fe<sub>3</sub>O<sub>4</sub>/graphene composites under UV and visible light at near neutral pH: effect of coexisting inorganic anion. *Environ. Nanotechnol. Monit. Manag.* **11**, 100221 (2019). <https://doi.org/10.1016/J.ENMM.2019.100221>
  23. Angkaew, A.; Chokejaroenrat, C.; Sakulthaew, C.; Mao, J.; Watcharatharapong, T.; Watcharenwong, A.; Imman, S.; Suriyachai, N.; Kreetachat, T.: Two facile synthesis routes for magnetic recoverable MnFe<sub>2</sub>O<sub>4</sub>/g-C<sub>3</sub>N<sub>4</sub> nanocomposites to enhance visible light Photo-Fenton activity for methylene blue degradation. *J. Environ. Chem. Eng.* **9**, 105621 (2021). <https://doi.org/10.1016/J.JECE.2021.105621>
  24. Jia, J.; Guo, X.; Zhang, T.; Zha, F.; Tang, X.; Tian, H.: Design of micro-nano spherical β-NiOOH/FeMoO<sub>4</sub> composite with enhanced Photo-Fenton performance. *Appl. Catal. A Gen.* **630**, 118427 (2022). <https://doi.org/10.1016/J.APCATA.2021.118427>
  25. Silva, E.D.N.; Brasileiro, I.L.O.; Madeira, V.S.; De Farias, B.A.; Ramalho, M.L.A.; Rodríguez-Aguado, E.; Rodríguez-Castellón, E.: Reusable CuFe<sub>2</sub>O<sub>4</sub>-Fe<sub>2</sub>O<sub>3</sub> catalyst synthesis and application for the heterogeneous Photo-Fenton degradation of methylene blue in visible light. *J. Environ. Chem. Eng.* **8**, 104132 (2020). <https://doi.org/10.1016/J.JECE.2020.104132>
  26. Mahdavinia, G.R.; Bazmizyynabad, F.; Seyyedi, B.: kappa-Carrageenan beads as new adsorbent to remove crystal violet dye from water: adsorption kinetics and isotherm. *Desalin. Water Treat.* **53**, 2529–2539 (2015). <https://doi.org/10.1080/19443994.2013.870741>
  27. Bakatula, E.N.; Richard, D.; Neculita, C.M.; Zagury, G.J.: Determination of point of zero charge of natural organic materials. *Environ. Sci. Pollut. Res.* **25**, 7823–7833 (2018). <https://doi.org/10.1007/s11356-017-1115-7>
  28. Langmuir, I.: The adsorption of gases on plane surfaces of glass, mica and platinum. *J. Am. Chem. Soc.* **40**, 1361 (1918). <https://doi.org/10.1021/ja02242a004>
  29. Freundlich, H.M.F.: Over the adsorption in solution. *J. Phys. Chem.* **57**, 385–471 (1906)
  30. Lagergren, S.K.: About the theory of so-called adsorption of soluble substances. *Sven Vetenskapsakad Handlingar* **24**, 1–39 (1898)
  31. Ho, Y.S.; McKay, G.: Pseudo-second order model for sorption processes. *Process Biochem.* **34**, 451–465 (1999). [https://doi.org/10.1016/S0032-9592\(98\)00112-5](https://doi.org/10.1016/S0032-9592(98)00112-5)
  32. Elovich, S.Y.; Zhabrova, G.M.: Mechanism of the catalytic hydrogenation of ethylene on nickel. I. Kinetics of the process. *J. Phys. Chem.* **13**, 1761 (1939)
  33. Sahmoune, M.N.: Evaluation of thermodynamic parameters for adsorption of heavy metals by green adsorbents. *Environ. Chem. Lett.* **17**, 697–704 (2019). <https://doi.org/10.1007/s10311-018-00819-z>
  34. Hassan, A.F.; Bulánek, R.: Preparation and characterization of thiosemicarbazide functionalized graphene oxide as nanoadsorbent sheets for removal of lead cations. *Int. J. Environ. Sci. Technol.* **16**, 6207–6216 (2019). <https://doi.org/10.1007/s13762-018-2002-6>
  35. Hassan, A.F.; Elhadidy, H.; Abdel-Mohsen, A.M.: Adsorption and photocatalytic detoxification of diaziron using iron and nanotitania modified activated carbons. *J. Taiwan Inst. Chem. Eng.* **75**, 299–306 (2017). <https://doi.org/10.1016/J.JTICE.2017.03.026>
  36. Haghightazadeh, A.; Hosseini, M.; Mazinani, B.: Kinetic and thermodynamic study of Trifluralin photo-degradation by ultra violet light You may also like Improved photocatalytic activity of ZnO-TiO<sub>2</sub> nanocomposite catalysts by modulating TiO<sub>2</sub> thickness. *Science* (2020). <https://doi.org/10.1088/1757-899X/454/1/012045>
  37. Ahile, U.J.; Wuana, R.A.; Itodo, A.U.; Sha' Ato, R.; Dantas, R.F.: Stability of iron chelates during Photo-Fenton process: the role of pH, hydroxyl radical attack and temperature. *J. Water Process Eng.* **36**, 101320 (2020). <https://doi.org/10.1016/J.JWPE.2020.101320>
  38. Mohammadnezhad, G.; Ariaeinezhad, F.; Steiniger, F.: Magnetite/κ-carrageenan nanocomposites: a convenient recyclable tool for Cu(II) ions adsorption from aqueous solution. *Inorg. Chem. Res.* **3**, 129–144 (2019). <https://doi.org/10.22036/icr.2020.209416.1056>
  39. Maciel, D.J.; Ferreira, I.L.D.M.; Da Costa, G.M.; Da Silva, M.R.: Nanocomposite hydrogels based on iota-carrageenan and maghemite: morphological, thermal and magnetic properties. *Eur. Polym. J.* **76**, 147–155 (2016). <https://doi.org/10.1016/J.EURPOLYMJ.2016.01.043>
  40. Petrie, F.A.; Gorham, J.M.; Busch, R.T.; Leontsev, S.O.; Ureña-Benavides, E.E.; Vasquez, E.S.: Facile fabrication and characterization of kraft lignin@Fe<sub>3</sub>O<sub>4</sub> nanocomposites using pH driven precipitation: effects on increasing lignin content. *Int. J. Biol. Macromol.* **181**, 313–321 (2021). <https://doi.org/10.1016/J.IJBIOMAC.2021.03.105>
  41. Wan, D.; Li, W.; Wang, G.; Wei, X.: Size-controllable synthesis of Fe<sub>3</sub>O<sub>4</sub> nanoparticles through oxidation-precipitation method as heterogeneous Fenton catalyst. *J. Mater. Res.* **31**, 2608–2616 (2016). <https://doi.org/10.1557/jmr.2016.285>
  42. Oun, A.A.; Rhim, J.W.: Carrageenan-based hydrogels and films: effect of ZnO and CuO nanoparticles on the physical, mechanical, and antimicrobial properties. *Food Hydrocoll* **67**, 45–53 (2017). <https://doi.org/10.1016/j.foodhyd.2016.12.040>
  43. Toledo, M.; Migo, V.; Alfafara, C.; Maguyon-Detras, M.C.; Brutas, C.C.: Process optimization for the production of potassium-carrageenan nanofertilizer by ionic crosslinking. *MATEC Web Conf.* **268**, 05002 (2019). <https://doi.org/10.1051/mateconf/201926805002>
  44. Mangione, M.R.; Giacomazza, D.; Bulone, D.; Martorana, V.; Cavallaro, G.; San Biagio, P.L.: K<sup>+</sup> and Na<sup>+</sup> effects on the gelation properties of κ-Carrageenan. *Biophys. Chem.* **113**, 129–135 (2005). <https://doi.org/10.1016/j.bpc.2004.08.005>
  45. Dindarloo, I.; Majnooni, S.; Eslahi, H.; Esmailpour, M.: Efficient nickel (II) immobilized on EDTA-modified Fe<sub>3</sub>O<sub>4</sub>@SiO<sub>2</sub> nanospheres as a novel nanocatalyst for amination of heteroaryl carbamates and sulfamates through the cleavage of C-O bond. *Mol. Catal.* **492**, 110915 (2020). <https://doi.org/10.1016/j.mcat.2020.110915>



46. Vigneshwaran, S.; Sirajudheen, P.; Poovathumkuzhi, C.: Photocatalytic performance of chitosan tethered magnetic Fe<sub>2</sub>O<sub>3</sub>-like (3D/2D) hybrid for the dynamic removal of anionic dyes: degradation and mechanistic pathways. *Int. J. Biol. Macromol.* **183**, 2088–2099 (2021). <https://doi.org/10.1016/j.ijbiomac.2021.06.012>
47. Hassan, A.F.; Elhadidy, H.: Effect of Zr<sup>4+</sup> doping on characteristics and sonocatalytic activity of TiO<sub>2</sub>/carbon nanotubes composite catalyst for degradation of chlorpyrifos. *J. Phys. Chem. Solids* **129**, 180–187 (2019). <https://doi.org/10.1016/j.jpcs.2019.01.018>
48. Deotale, A.J.; Nandedkar, R.V.: Correlation between particle size, strain and band gap of iron oxide nanoparticles. *Mater Today Proc.* **3**, 2069–2076 (2016). <https://doi.org/10.1016/j.matpr.2016.04.110>
49. Bagbi, Y.; Sarswat, A.; Mohan, D.; Pandey, A.; Solanki, P.R.: Lead and chromium adsorption from water using L-cysteine functionalized magnetite (Fe<sub>3</sub>O<sub>4</sub>) nanoparticles. *Sci. Rep.* **7**, 1–15 (2017). <https://doi.org/10.1038/s41598-017-03380-x>
50. Vieira, Y.; Silvestri, S.; Leichtweis, J.; Luiz, J.S.; Marlonde, M.F.É.; Luiz, D.G.; Luiz, F.E.: New insights into the mechanism of heterogeneous activation of nano-magnetite by microwave irradiation for use as Fenton catalyst. *J. Environ. Chem. Eng.* **8**, 103787 (2020). <https://doi.org/10.1016/j.jece.2020.103787>
51. Zharmagambetova, A.K.; Talgatov, E.T.; Auyezkhanova, A.S.; Tumabayev, N.Z.; Bukharbayeva, F.U.: Effect of polyvinylpyrrolidone on the catalytic properties of Pd/γ-Fe<sub>2</sub>O<sub>3</sub> in phenylacetylene hydrogenation. *React. Kinet. Mech. Catal.* **131**, 153–166 (2020). <https://doi.org/10.1007/s11144-020-01857-x>
52. Vunain, E.; Mishra, A.K.; Krause, R.W.: Ethylene-vinyl acetate (EVA)/polycaprolactone (PCL)-Fe<sub>3</sub>O<sub>4</sub> composites: preparation, thermal and mechanical properties. *J. Therm. Anal. Calorim.* **114**, 791–797 (2013). <https://doi.org/10.1007/s10973-013-3004-8>
53. Selim, M.S.; Elmarakbi, A.; Azzam, A.M.; Shenashen, M.A.; El-Saeed, A.M.; El-Safty, S.A.: Eco-friendly design of superhydrophobic nano-magnetite/silicone composites for marine foul-release paints. *Prog. Org. Coat.* **116**, 21–34 (2018). <https://doi.org/10.1016/j.porgcoat.2017.12.008>
54. Sangeetha, J.; Philip, J.: Synthesis, characterization and antimicrobial property of Fe<sub>3</sub>O<sub>4</sub>-Cys-HNQ nanocomplex, with L-cysteine molecule as a linker. *RSC. Adv.* **3**, 8047–8057 (2013). <https://doi.org/10.1039/c3ra00005b>
55. Din, S.U.; Ajmal, A.; Zain-Ul, A.; Haq, S.; Muhammad, H.; Imran, M.; Hussain, S.; Saleh, A.S.: Investigation on cadmium ions removal from water by a nanomagnetite based biochar derived from *eleocharis dulcis*. *J. Inorg. Organomet. Polym. Mater.* **31**, 415–425 (2021). <https://doi.org/10.1007/s10904-020-01758-5>
56. Kaith, B.S.; Jindal, R.; Mittal, H.; Kumar, K.: Temperature, pH and electric stimulus responsive hydrogels from Gum ghatti and polyacrylamide-synthesis, characterization and swelling studies. *Der Chemica Sinica.* **1**, 44–54 (2010)
57. Sebeia, N.; Jabli, M.; Ghith, A.; Elghoul, Y.M.; Alminderej, F.: Production of cellulose from *Aegagropila Linnaei* macroalgae: chemical modification, characterization and application for the bio-sorption of cationic and anionic dyes from water. *Int. J. Biol. Macromol.* **135**, 152–162 (2019). <https://doi.org/10.1016/J.IJBIOMAC.2019.05.128>
58. Abebe, B.; Ananda Murthy, H.C.; Zerefa, E.; Abdisa, E.: Porous PVA/Zn-Fe-Mn oxide nanocomposites: methylene blue dye adsorption studies. *Mater. Res. Express* **7**, 065002 (2020). <https://doi.org/10.1088/2053-1591/ab94fc>
59. Gemici, B.T.; Ozel, H.U.; Ozel, H.B.: Removal of methylene blue onto forest wastes: adsorption isotherms, kinetics and thermodynamic analysis. *Environ. Technol. Innov.* **22**, 101501 (2021). <https://doi.org/10.1016/j.eti.2021.101501>
60. Kamal, K.H.; Dacrory, S.; Ali, S.S.M.; Ali, K.A.; Kamel, S.: Adsorption of Fe ions by modified carrageenan beads with tricarboxy cellulose: kinetics study and four isotherm models. *Desalin. Water Treat.* **165**, 281–289 (2019). <https://doi.org/10.5004/dwt.2019.24560>
61. Amrhar, O.; Nassali, H.; Elyoubi, M.S.: Adsorption of a cationic dye, methylene blue, onto moroccan illitic clay. *J. Mater. Environ. Sci.* **6**, 3054–3065 (2015)
62. Zhang, Z.; Xu, L.; Liu, Y.; Feng, R.; Zou, T.; Zhang, Y.; Kang, Y.; Zhou, P.: Efficient removal of methylene blue using the mesoporous activated carbon obtained from mangosteen peel wastes: kinetic, equilibrium, and thermodynamic studies. *Microporous Mesoporous Mater.* **315**, 110904 (2021). <https://doi.org/10.1016/j.micromeso.2021.110904>
63. Hassan, A.F.; El-Naggar, G.A.; Braish, A.G.; Amira, M.F.; Alshandoudi, L.M.: Enhanced adsorption of chromium(VI) from aqueous medium by basic nanohydroxyapatite/chitosan composite based on egg shell. *Desalin. Water Treat.* **206**, 235–249 (2020). <https://doi.org/10.5004/dwt.2020.26306>
64. Shi, Z.; Zhang, R.; Zhang, J.: Role of weak magnetic field for enhanced oxidation of orange G by magnetic Fenton. *Environ. Sci. Pollut. Res.* **2**, 1–10 (2021). <https://doi.org/10.1007/s11356-021-14887-2>
65. Fayazi, M.: Preparation and characterization of carbon nanotubes/pyrite nanocomposite for degradation of methylene blue by a heterogeneous Fenton reaction. *J. Taiwan Inst. Chem. Eng.* **120**, 229–235 (2021). <https://doi.org/10.1016/j.jtice.2021.03.033>
66. Daud, N.K.; Hameed, B.H.: Decolorization of Acid Red 1 by Fenton-like process using rice husk ash-based catalyst. *J. Hazard. Mater.* **176**, 938–944 (2010). <https://doi.org/10.1016/j.jhazmat.2009.11.130>
67. Sun, S.P.; Lemley, A.T.: P-Nitrophenol degradation by a heterogeneous Fenton-like reaction on nano-magnetite: process optimization, kinetics, and degradation pathways. *J. Mol. Catal. A Chem.* **349**, 71–79 (2011). <https://doi.org/10.1016/j.molcata.2011.08.022>
68. Liu, S.T.; Huang, J.; Ye, Y.; Zhang, A.B.; Pan, L.; Chen, X.G.: Microwave enhanced Fenton process for the removal of methylene blue from aqueous solution. *Chem. Eng. J.* **215–216**, 586–590 (2013). <https://doi.org/10.1016/J.CEJ.2012.11.003>
69. Hu, S.; Yao, H.; Wang, K.; Lu, C.; Wu, Y.: Intensify removal of nitrobenzene from aqueous solution using nano-zero valent iron/granular activated carbon composite as Fenton-like catalyst. *Water Air Soil Pollut.* **226**, 1–13 (2015). <https://doi.org/10.1007/s11270-015-2421-7>
70. Jain, J.; Ajaya, B.; Singh, K.; Kim, H.; Lichtfouse, E.; Sharma, V.K.: Treatment of organic pollutants by homogeneous and heterogeneous Fenton reaction processes. *Environ. Chem. Lett.* **16**, 947–967 (2018). <https://doi.org/10.1007/s10311-018-0738-3>
71. Raheb, I.; Manlla, M.S.: Kinetic and thermodynamic studies of the degradation of methylene blue by Photo-Fenton reaction. *Heliyon.* **7**, e07427 (2021). <https://doi.org/10.1016/J.HELIYON.2021.E07427>
72. Khan, J.; Tariq, M.; Muhammad, M.; Mehmood, M.H.; Ullah, I.; Raziq, A.; Akbar, F.; Saqib, M.; Rahim, A.; Niaz, A.: Kinetic and thermodynamic study of oxidative degradation of acid yellow 17 dye by Fenton-like process: effect of HCO<sub>3</sub><sup>-</sup>, CO<sub>3</sub><sup>2-</sup>, Cl<sup>-</sup> and SO<sub>4</sub><sup>2-</sup> on dye degradation. *Bull. Chem. Soc. Ethiop.* **33**, 243–254 (2019). <https://doi.org/10.4314/bcse.v33i2.5>
73. Chang, J.; Ma, J.; Ma, Q.; Zhang, D.; Qiao, N.; Hu, M.; Ma, H.: Adsorption of methylene blue onto Fe<sub>3</sub>O<sub>4</sub>/activated montmorillonite nanocomposite. *Appl. Clay Sci.* **119**, 132–140 (2016). <https://doi.org/10.1016/j.clay.2015.06.038>
74. Shahnaz, T.; Bedadeep, D.; Narayanasamy, S.: Investigation of the adsorptive removal of methylene blue using modified nanocellulose. *Int. J. Biol. Macromol.* **200**, 162–171 (2022). <https://doi.org/10.1016/j.ijbiomac.2021.12.081>



75. Izghri, Z.; Enaime, G.; Eouarrat, M.; Chahid, L.; El Gaini, L.; Baçaoui, A.; Yaacoubi, A.: Hydroxide sludge/hydrochar-Fe composite catalysts for photo-Fenton degradation of dyes. *J. Chem.* **2021**, 1–12 (2021). <https://doi.org/10.1155/2021/5588176>
76. Bavarsiha, F.; Rajabi, M.; Montazeri-Pour, M.: Synthesis of SrFe<sub>12</sub>O<sub>19</sub>/SiO<sub>2</sub>/TiO<sub>2</sub> composites with core/shell/shell nanostructure and evaluation of their photo-catalytic efficiency for degradation of methylene blue. *J. Mater. Sci. Mater. Electron* **29**, 1877e1887 (2018). <https://doi.org/10.1007/s10854-017-8098-5>
77. Behnood, R.; Sodeifian, G.: Synthesis of Ag<sub>4</sub>Bi<sub>2</sub>O<sub>5</sub> nanoparticles and evaluation of their photocatalytic activity. *J. Photochem. Photobiol. A Chem.* **427**, 113776 (2022). <https://doi.org/10.1016/j.jphotochem.2022.113776>
78. Lu, R.; Wang, C.; Chen, Y.; Tan, L.; Wang, P.; Feng, S.: IL-functionalized Mn(II)-doped core-shell Fe<sub>3</sub>O<sub>4</sub>@Zr-MOF nanomaterials for removal MB from wastewater based on dual adsorption/Fenton catalysis. *New J. Chem.* **2**, 8534–8544 (2022). <https://doi.org/10.1039/d2nj00651k>
79. Hromádka, L.; Motola, M.; Čičmancová, V.; Bulánek, R.; Macak, J.M.: Facile synthesis of WO<sub>3</sub> fibers via centrifugal spinning as an efficient UV- and VIS-light-driven photocatalyst. *Ceram. Int.* **47**, 35361–35365 (2021). <https://doi.org/10.1016/j.ceramint.2021.09.079>

